

https://dspace.org/

Iron supported on Clinoptilolite (natural zeolites) as a low-temperature Fischer-Tropsch synthesis catalyst

Chikati, Roick

2019

https://hdl.handle.net/10539/28773

Chikati, Roick(2019) Iron supported on Clinoptilolite (natural zeolites) as a low-temperature Fischer-Tropsch synthesis catalyst, University of the Witwatersrand, Johannesburg, <http://hdl.handle.net/10539/28773>

Downloaded from a DSpace repository. https://dspace.org/

Iron supported on Clinoptilolite (natural zeolites) as a low-temperature Fischer-Tropsch synthesis catalyst

---

Prepared by

Roick Chikati

Submitted to

School of Chemical and Metallurgical Engineering, Faculty of Engineering and the Built Environment, University of the Witwatersrand, Johannesburg, South Africa

Supervisor: Dr D Nkazi

Co-Supervisor: Dr J Gorimbo

May, 2019

DECLARATION

I declare that this dissertation is my own unaided work. It is being submitted for the Degree of Master of Science to the University of the Witwatersrand, Johannesburg. It has not been submitted before for any degree or examination to any other University.

_____ on this ____ day of _____

(Candidate)

ABSTRACT

In the Fischer-Tropsch (FT) synthesis, CO and H_2 (synthesis gas) are converted into plethora of hydrocarbons mainly paraffins and olefins and these can be further upgraded to high-quality fuels and chemicals. Different carbon sources such as natural gas, coal and biomass can be used as feed-stocks for the synthesis gas. In commercial applications, precipitated and fused iron catalysts are commonly used in the Fischer-Tropsch synthesis, especially when the synthesis gas emanates from coal or biomass where the CO/H_2 needs adjustments via the WGS reaction and when the desired final products are mainly olefins. However, there was a problem associated with the catalyst's mechanistic resistance; also, these types of Fe catalysts consume large amounts of iron resource. Development of cheap, efficient and robust support iron catalyst become an urgent task

Zeolites and zeolite rocks are commonly used in different industrial applications. Natural zeolites present an attractive material as supports in FTS because of their high abundance, availability, low costs and their properties. Detailed mineralogical knowledge and profound characterization of natural zeolites are essential for fitting chemical composition to use. Si/Al ratios are very import as well as the other contaminates. A fundamental difference exists between commercial supports such as silica and alumina - with functional porous materials - and natural supports such as zeolites. In this study natural zeolite called clinoptilolite (a type of zeolite found in South Africa) was used as a catalyst support. This support proved to be promising for low-temperature Fischer–Tropsch synthesis (LTFTS) targeting liquid fuel production, as well as chemical feedstock. Synthesis of this highly active catalyst was by loading of iron on clinoptilolite through the wet impregnation method. The prepared catalyst was then characterized by XRF, BET surface area analyzer, XRD and SEM. The catalyst was then loaded into the reactor and reduced with hydrogen prior to FTS. The effects of its use as support in FTS were investigated in a fixed bed reactor.

From the XRF results the molecular ratio SiO_2/ Al_2O_3 of the Clino-support was 5.86. The average crystal size of the particles from both HRTEM and XRD ranged 9.8 -11.6 nm and around 10.10nm for used and fresh catalyst. It was found that the CO consumption rate of 1.02×10^{-4} mol/min.gcat of which 7.24×10^{-5} mol/min.gcat was the actual Fischer Tropsch

rate with the remaining 2.93 x 10^{-5} mol/min.gcat consumed by the WGS reaction. The product distribution of the gaseous phase analysed were more olefinic than paraffinic. The product distribution for this condition follows a one alpha ASF distribution with an alpha value of 0.86. These findings may permit the development of new effective support materials, which are cost effective for clean fuel production via FTS process.

ACKNOWLEDGEMENTS

First of all, I would like to thank GCC for the financial support, without it this work would not have been possible. I feel very grateful to my supervisors' Dr D Nkazi and Dr J Gorimbo for giving me the opportunity to carry out postgraduate studies at the university of Witwatersrand department of chemical and metallurgical engineering. I am very grateful to Diemo for improving the linguistic quality of this thesis. Thanks to my family for all the love.

TABLE OF CONTENTS

Section ***Page***

Declaration....i

Abstract....ii

Acknowledgements....iv

Table of contents....v

List of figures....viii

List of abbreviations....x

CHAPTER 1 INTRODUCTION....1

1.1 Introduction....1

1.1.1 The major difference between natural and synthesis zeolites....6

1.1.2 Overview of the catalyst reduction process....7

1.2 Research justification....8

1.3 Research objectives....8

1.4 Dissertation outcome....9

1.5 Dissertation outline....9

References....11

CHAPTER 2 LITERATURE REVIEW....13

2.1 Introduction....13

2.2 Support materials....13

CHAPTER 1....14

2.2.1 Conventional supports....15

2.2.2 Non-conventional....17

2.2.3 Structural characteristics of the studied Clinoptilolite....17

2.2.4 Synthetic zeolites 18
2.3 Natural versus synthetic supports 20
2.4 Catalyst preparation 21
2.5 Catalyst pre-treatment 22
2.6 Iron Based Fischer-Tropsch Catalyst 24
2.7 Thermal conductivity 25
2.8 Anderson-Schulz-Flory Model 28
2.9 Yao plots 30
References 32

CHAPTER 3 EXPERIMENTAL METHODOLOGY 37

3.1 Introduction 37
3.2 Material and chemicals 37
3.2.1 Catalyst preparation 38
3.2.2 Catalyst characterization 39
3.3 Experimental setup 41
3.3.1 FTS reactors 44
3.3.2 Catalyst loading into the disassembled reactor 44
3.4 Fischer-Tropsch and catalyst evaluation 46
3.4.1 Catalyst reduction procedure 46
3.4.2 FT synthesis 46
3.4.2.1 Product separation and analysis 47
3.4.2.2 Product storage 51
3.4.2.3 Calculation 51
References 55

CHAPTER 4 RESULTS AND DISCUSSION 56

4.1 Characterization of fresh prepared catalysts 56
4.1.1 Temperature programmed reduction 56
4.1.2 X-ray fluorescence characterization of natural zeolite 58
4.1.3 X-ray Diffraction 59

4.1.4 High resolution Transmission Electron Microscopy (HRTEM) 61
4.1.5 Brunauer-Emmett-Teller (BET) 62
4.2 FT results 64
4.2.1 Catalytic activity 64
4.2.2 Rates 65
4.2.3 Ratios 70
4.2.4 The relationship between $P_{(n+1)}/O_{(n+1)}$ and $P_{(n)}/O_{(n)}$ 72
References 76

CHAPTER 5 Conclusions and recommendations 78

5.1 Conclusions 78
5.2 Recommendations 79

LIST OF FIGURES

Figure	***Description***	***Page***
Figure 1.1:	Generic block diagram of the FT plant process including syngas product and FTS. The parts in red show areas for potential savings.	2
Figure 1.2:	Natural zeolite granules. (Samples collected from Pratley Krugersdrop)	4
Figure 1.3:	Variation of porosity of natural zeolites with bulk density[37].	5
Figure 1.4:	SEM images of natural zeolite at different magnification[36]	6
Figure 1.5:	An alternative way of predicting phase evolution of iron-based Fischer Tropsch synthesis catalysts during activation[18].	7
Figure 2.1:	Catalyst preparation steps.	21
Figure 2.2:	Typical TPR profiles for the calcined and unreduced catalysts 10 wt.% Co/TiO2[76] (Co3O4 to Co).	22
Figure 2.3:	FTS reduction temperatures for cobalt based catalyst.	23
Figure 2.5:	Plot of the ratio of P(n + 1)/O(n + 1) as a function of the ratio of Pn/On for FTS[101].	31
Figure 3.1: Flow scheme of the laboratory scale Fischer Tropsch rig with fixed bed reactor.		42
Figure 3.2: Schematic representation of the fixed bed reactor used in this study [6].		44
Figure 3.3: Representation of the FT reactor loaded with catalyst		45
Figure 3.4: Typical online analysis of the syngas (red line from TCD detector and blue line from that of FID)		50
Figure 3.5: Typical online analysis of the calibration gas (red line from TCD detector and blue line from FID)		50
Figure 3.6: Typical online analysis of the tail gas (red line from TCD detector and blue line from FID)		50
Figure 4.1: H2 TPR profiles of the calcined Iron catalysts		56

Figure 4.2: X-ray diffraction patterns of Natural Clinoptilolite and Fe- Clinoptilolite catalyst 60

Figure 4.3: HRTEM images of the (a,b) fresh catalysts at 20 nm and 10 nm respectively and (c) used catalyst at 5 nm. 61

Figure 4.4: CO conversion, WGS selectivity and FT selectivity under operating conditions: 250 °C, 2592 h-1 at 20.85 bar (abs). 64

Figure 4.5: CO consumption rate, WGS rate and FTS rate under operating conditions: 250 °C, 2592 h-1 at 20.85 bar (abs)..... 67

Figure 4.6: Paraffin production rate(left) and olefins production rate (right) for TOS of 450 h. 68

Figure 4.7: Paraffin/Olefin ratios under the following FT reaction condition: 250 ^{0}C, 2592 h-1, 20.85 bar (absolute), syngas (H2:CO = 2 mol/mol) 70

Figure 4.8: Wave like behavior of light hydrocarbon selectivity distribution 71

Figure 4.9: Typical gas chromatogram of the tail gas collected from the FTS experiment in this study. 72

Figure 4.10: Yao Plots for $P_{(n+1)}/O_{(n+1)}$ versus P_n/O_n with carbon number n = 2–5 73

Figure 4.11: ASF distribution for light hydrocarbons 75

LIST OF ABBREVIATIONS, NOMENCLATURES AND SYMBOLS

Abs	Absolute
Afrox	African Oxygen Limited
ASF	Anderson–Schultz–Flory
BET	Brunauer–Emmett–Teller
BTL	Biomass to liquid
Fe-Clino	Iron supported on Clinoptilolite
CO	Carbon monoxide
CTL	Coal to liquid
EXAFS	Extended X-ray absorption fine structure
FBR	Fixed bed reactor
Fe	Iron
FID	Flame ionisation detector
FT	Fischer Tropsch
FTS	Fischer Tropsch synthesis
GC	Gas chromatograph
GHSV	Gas hourly space velocity
GTL	Gas to liquid
H_2	Hydrogen
HTFT	High temperature Fischer Tropsch
mL/min	Millilitre per minute
mol/min	Mole per minute
N	Carbon number
N_2	Nitrogen

NTP	Normal temperature and pressure
OD	Outside diameter
P	Pressure
P&ID	Piping and instrumentation diagram
Syn	Syngas
SA	Surface area
SASOL	South African Coal, Oil and Gas Corporation
SEM	Scanning electron microscopy
T	Temperature
TCD	Thermal conductivity detector
TEM	Transmission electron microscopy
TGA	Thermo gravimetric analysis
TOS	Time on stream
TPR	Temperature-programmed reduction
UHP	Ultra high purity
VLE	Vapour-liquid equilibrium
WGS	Water-gas shift
Wn	Mass fraction of the species with carbon number n
XPS	X-ray photoelectron spectroscopy
XRD	X-ray diffraction
α	Chain growth probability

CHAPTER 1

INTRODUCTION

1.1 Introduction

Fischer-Tropsch synthesis (FTS) is basically the conversion of carbon containing feedstock over a metal catalyst into liquid fuel, chemicals and water. The technology is often referred to as X-to-liquid (XTL) because X represents any carbon-based material, such as natural gas, coal or biomass. Synthesis gas (syngas) originates from natural gas, coal or biomass through processes such as reforming for methane gas [1], or gasification for coal and biomass [2–5]. XTL technology designates the conversion of gas-to-liquids (GTL), coal-to-liquids (CTL) or biomass-to-liquids (BTL), which refers to the starting source of carbon. Syngas is a mixture of carbon monoxide (CO), hydrogen (H_2) and nitrogen (N_2) which is used as the feed for FTS. Syngas with a stoichiometric ratio (H_2/CO) of 2 (or ranging from 1 to 2) is generally obtained depending on the feedstock and process used. The feed ratio chosen for FT processes influences the resultant products.

The FTS process yields a wide spectrum of products, with olefins and paraffin being the most desired ones. In addition, fractions of oxygenates are obtained. Large quantities of water are produced as a by-product [6,7]. The main reactions of FTS are represented by equations (1.1) to (1.3):

$$n\mathrm{CO} + (2n + 1)\mathrm{H_2} \rightarrow \mathrm{C_nH_{2n+2}} + n\mathrm{H_2O} \quad (1.1)$$

$$n\mathrm{CO} + 2n\mathrm{H_2} \rightarrow \mathrm{C_nH_{2n}} + n\mathrm{H_2O} \quad (1.2)$$

$$n\mathrm{CO} + 2n\mathrm{H_2} \rightarrow \mathrm{C_nH_{2n+2}O} + (n - 1)\mathrm{H_2O} \quad (1.3)$$

FTS process has been of interest to researchers in industries and academia because it represents an alternative method of producing transportation fuels. Figure 1 depicts the process flow diagram for the whole FT process, which consists of three main sections:

gasification, FTS and products upgrading. The flow diagram illustrates the conditions commonly used at industrial scale.

The first sections are dependent on the feedstock. The second step the synthesis gas is converted into a variety of hydrocarbons with different chain lengths, which will depend on the catalyst and the process parameters. Some of the FT products can be directly used for food, cosmetics and medical applications. If high quality fuels are required, Fischer-Tropsch wax is hydrocracked. The process itself has proved to be a satisfying alternative for the production of fuels in regions where crude oil is scarce while other carbonaceous sources are abundant.

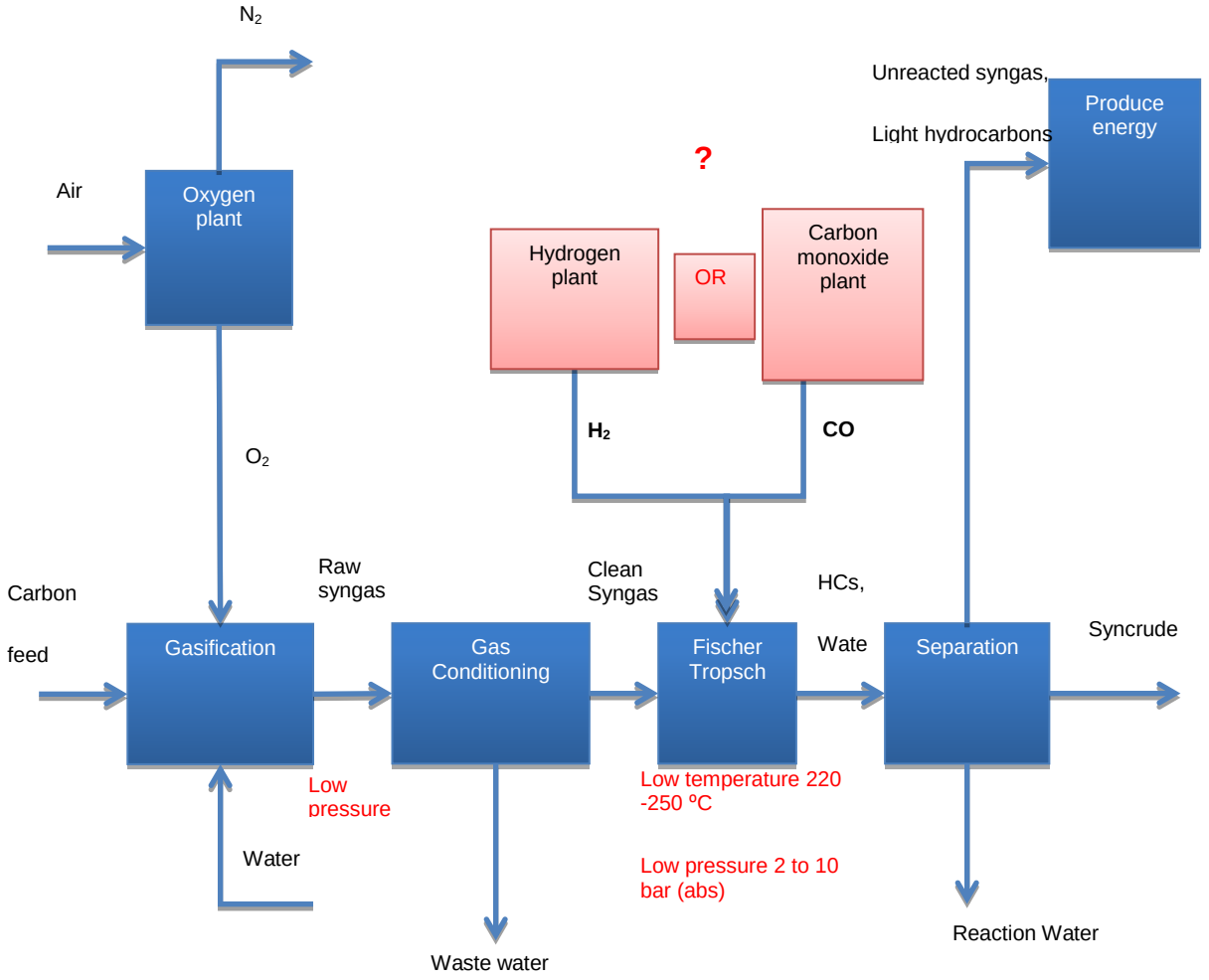


Figure 1.1: Generic block diagram of the FT plant process including syngas product and FTS. The parts in red show areas for potential savings.

There are two modes of FTS operation namely High Temperature Fischer Tropsch (HTFT) (300 ℃ -350 ℃, 20 -40 bars, H_2 / CO « 2) and Low Temperature Fischer Tropsch (LTFT) (200 ℃ -240 ℃, 20 -45 bars, H_2 / CO = 1.7 -2.15)[3,8–12]. Reactor systems or configurations mainly used commercially include tubular fixed bed reactor, circulating fluidized bed reactor, slurry phase reactor and a fluidized bed reactor [11,13–15].

Research conducted thus far has endeavored to optimize each stage in an attempt to improve production and lower the operation cost. Furthermore, the literature shows that several studies have focused on the effect of FT operating parameters, including feed sources, type catalysts and catalyst supports [8,16–21]. This study intends to extend the investigation and focus specifically on the effect of catalyst supports in a naturally available material (zeolite) for FT process. The choice of the catalyst is governed by factors such as cost and the selectivity of the desired products. Iron and cobalt are the most used metal-based FT catalysts in the industry. For instance, currently all the commercial Sasol FT units are operating with Fe-based catalysts, developed and manufactured in their own facilities [12]. Iron based catalysts have been widely used because of their low cost and availability. It is reported that iron is the most abundant element in the Earth (measured by mass), constituting about 80% of the inner and outer cores of the Earth [22]. It is this ubiquitous nature of iron that provides the researcher with the impetus to develop an iron catalyst supported on cheap naturally occurring zeolites. Catalyst supports such as silica and alumina play an important role on the structure of the iron catalyst, with significant effects on the activity and selectivity during FTS [23]. Furthermore, iron catalysts are preferred over cobalt, coal or biomass for FTS because of their cost effectiveness, low methane selectivity and high water–gas shift (WGS) activity. WGS activity is needed for the internal production of H_2 during FTS because of the inherently low H_2/CO ratios of syngas produced from coal or biomass [24].

Many inorganic oxides such as silica (SiO_2) [25] , alumina (Al_2O_3) [26], titania (TiO_2) [27] and silicon carbide [28] have been studied as supports for Fe catalysts. However, significant support interactions on the reduction of cobalt oxide species were observed in this order: $Al_2O_3 > TiO_2 > SiO_2$ [29]. These interactions often make the catalyst difficult to reduce when highly dispersed on refractory oxides. Addition of reduction promoter is therefore done to enhance catalyst reducibility.

Recently, researchers have reported interesting findings when zeolite supported FT catalysts were employed [24–26]. Zeolites are known to have great potential as catalysts or catalyst supports because of their properties, such as high surface area, high porosity, high adsorption capacity and ease of separation from reactant products. One of the natural zeolite deposits in South Africa has been found to have a large silica content of approximately 69% [34] at a unique deposit site. Zeolite minerals are often found in the volcanic tuffs of the Heidelberg-Riversdale area in the Western Cape, as well as in the volcanic tuffs of Nxwala Estate in the Northern KwaZulu-Natal, South Africa [35].

X- ray fluorescence studies done on South African zeolite reveals that the zeolite consists of all the phases of material used as supports and promoters in FTS catalyst [34]. Adding supporters to aid catalyst reducibility and activity metals such as alkali metals would not be necessary since they are already contained in the natural zeolite. South African zeolite contains promoter percentages that are almost identical to those recommended in FTS catalyst [36].



Figure 1.2: Natural zeolite granules. (Samples collected from Pratley Krugersdrop)

Zeolites in nature often, formed as crystals in small cavities of basaltic rocks over the years or as volcanic tuffs or glass altered by the interaction with saline water. These natural zeolites are formed in a number of geological environments such as alkaline deserts, lake sediments, ash ponds and marine sediments at relatively low temperature, under natural conditions[37]. Zeolites are distinguished by differences in their chemical compositions and the sizes and arrangement of their crystal structure. Clinoptilolite is the most commonly mined natural zeolite in South Africa and an example of the mined clinoptilolite is given in **Figure 1.2**.

The most general physical properties of the zeolites are bulk density and specific gravity (i.e., somewhere in between 2 and 2.4)[37], which can correlate with their porosity (i.e., the measure of the pore volume in zeolite). For example, the observed trends of variations such as one between porosity and specific gravity are exhibited by **Figure 1.3**. It can be noted that there is negligible change in specific gravity with increase in porosity of zeolites (viz., Analcime, Mordenite, Philipsite, Clinoptilolite, Erionite, Heulandite and Chabazite).

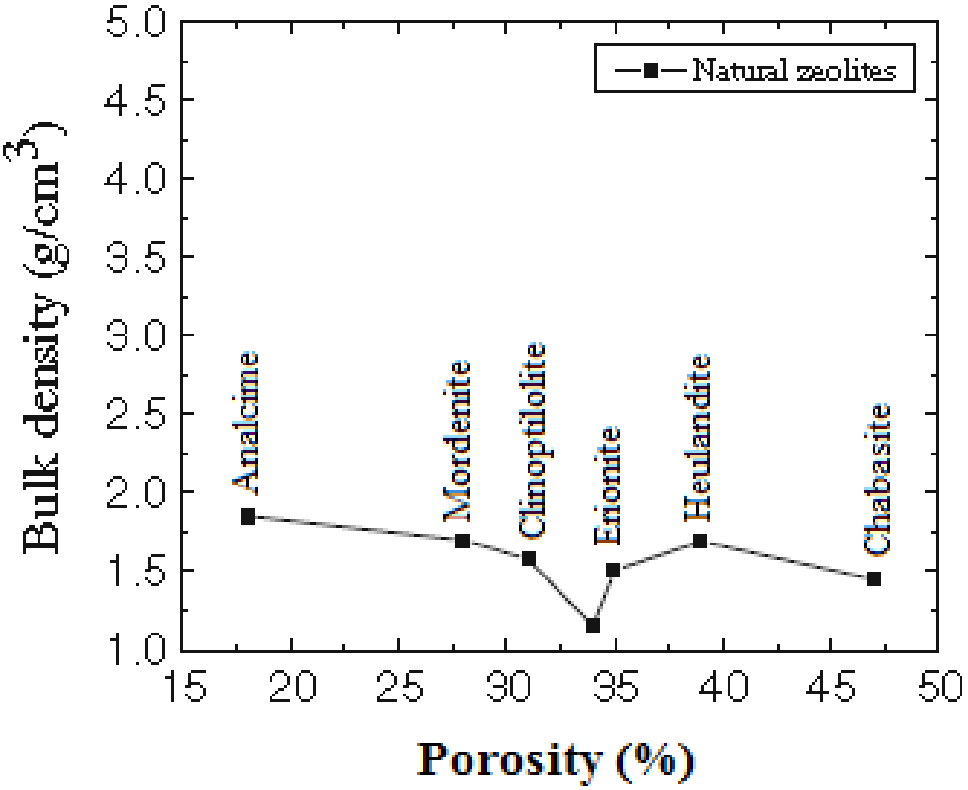


Figure 1.3: Variation of porosity of natural zeolites with bulk density[37].

Clinoptilolite itself will also vary in composition from one source to another, mainly with regard to the inter-changeable ions viz. Na^+, K^+, Ca^{2+} and Mg^{2+}. Thus, they are referred to as sodium, potassium, calcium and magnesium clinoptilolites.

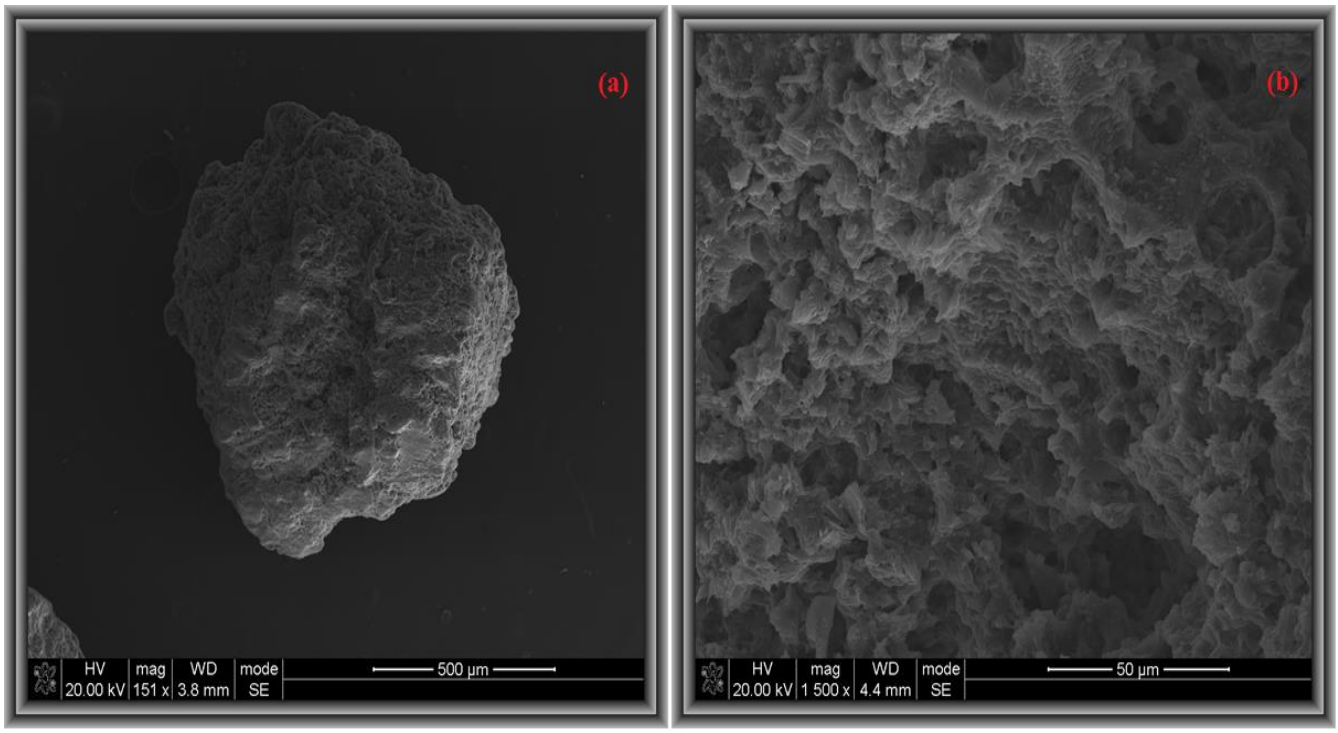


Figure 1.4: SEM images of natural zeolite at different magnification[36]

SEM is widely used to study the morphological features and surface characteristics of the adsorbent materials. Visual examination of natural and pretreated clinoptilolite specimens by FEI Nova FIB/SEM reveals important information on the surface structure, shape and shows the distribution of micro and mesopores. **Figure 1.4** are SEM photomicrographs of natural clinoptilolite clearly showing micropores at 1500 magnification[36]. The natural form is found to be largely covered with foreign materials on the surface which could be impurities or very fine zeolite particles.

1.1.1 **The major difference between natural and synthesis zeolites**

The main differences between natural and synthetic zeolites are the time scale in which the y are produced, the amount of material used to produce them and the quality of zeolites. Natural zeolites have many more chemical elements in its structure [36], and they are

found in many geological environments hence they have much greater structural and crystal chemical variability than synthetic zeolites. Synthetic zeolites can be created in few hours or few days in the laboratory whereas natural zeolites can be generated in years or a million years.

Clearly a synthetic compound has a chemical composition made of the ingredients used in the synthesis, hence well known composition to the producer. The production of a synthetic zeolite is also aimed at providing the material with certain wanted properties i.e. it tends to be tailored to specific industrial needs. Whereas a natural zeolite is made of the most common mineral-forming elements and it's composition may vary not only from a mineral species to another but also within the same mineral species.

1.1.2 **Overview of the catalyst reduction process**

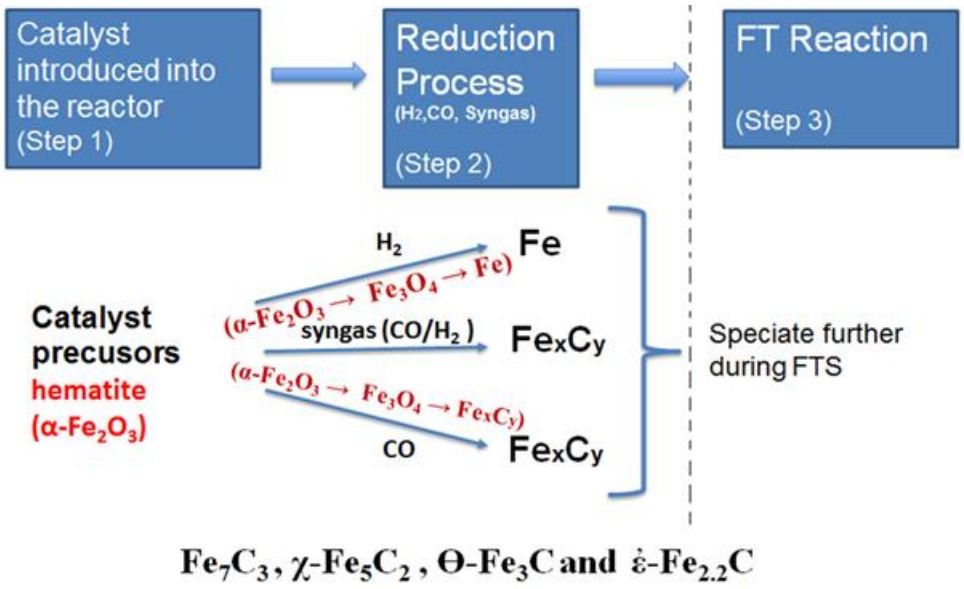


Figure 1.5: An alternative way of predicting phase evolution of iron-based Fischer Tropsch synthesis catalysts during activation[18].

After catalyst preparation, the reduction of it is usually done in situ. In the case of iron-based catalyst three different reducing gases (see figure 1.5) have been used and found to be almost equally effective[38]. This study will make use of hydrogen reduction.

1.2 Research justification

Catalyst support is as important as the metals deposited on them, as this influences several factors including the activity, selectivity, catalyst stability and the costing of the catalyst. However, presently most of the catalyst supports used in FTS are commercially synthesized. Natural zeolites (Clinoptilolite, which is mined in South Africa) have the physico-chemical properties of a good support [34], an adequate phase makeup and other constituents congruent with commercial supports. Moreover, the deactivation modes of these natural zeolite supported catalysts are not as well studied as commercial supports. It is therefore warranted that a comprehensive investigation is undertaken to shed light on natural zeolite supported FT catalysts. As a result, the cost of the catalyst could perhaps be lowered below the conventional power generating systems despite the benefits of higher efficiency and cleaner environment.

1.3 Research objectives

This dissertation seeks to probe explorations of catalyst design aim to make an affordable, highly active and selective, as well as stable catalyst. Some of the most important variables include the selection of the metal precursor, metal loading, support characteristics, promoters, preparation and catalyst activation method. The iron-support characteristics may influence the physicochemical properties of the deposited iron particle such as: particle size, degree of reduction, dispersion, metal-support interaction among others; and as a consequence the performance of the final catalyst in the Fischer-Tropsch reaction.

This aim would be achieved via the following outlined activities and objectives:

- To study the effect of natural zeolite as support on the activity and selectivity of impregnated iron catalyst in FT synthesis using a tubular fixed bed reactor.

- To study the interaction of the loaded metal with the support and the effect of carbon deposition on the porosity of the natural zeolite supported iron FT catalyst.

- To study the speciation of various phases making up the natural zeolite and the effect of this speciation on the activity of the FT catalyst.

- To compare the thermal conductivity of various commercially available support with the natural zeolite.

- To develop a preliminary toolbox for improved zeolite supported iron FT catalyst and FT reactor efficiency based on experimental data and fundamental thermodynamic principles.

The experimental work included constructing the FT rig, reducing the iron catalyst at atmospheric pressure, 250 ^{o}C, and a gas hourly space velocity (GHSV) of 2592 h^{-1} with H_2 as reducing gas. The actual FTS was then carried out.

1.4 Dissertation outcome

The outcome of this work is expected to contribute towards a better understanding of naturally occurring zeolite supports used in FT catalyst, and the influence that this will have on the product distribution. This research work is expected to provide a strong basis for further work on the use of natural zeolites with and without further modification to create FT catalysts with desirable properties, activity and selectivity to products.

1.5 Dissertation outline

The work presented in this thesis is organised in five chapters. The current chapter has presented the background, problem statement, research justification, research objectives and scope (outline) for the research work to follow.

Chapter 1: gives a short background on FTS, the research problem, the aims and objectives, and the scope and outline of the research.

Chapter 2: presents a review of the literature on Fischer Tropsch synthesis paying particular attention to the support used and their effect in the behaviour of the catalyst. The areas where information is still lacking are highlighted. Hence, this chapter provides a context for the research work to follow.

Chapter 3: describes the experimental equipment and the measuring system components used in the work undertaken for the research as well as the programs involved and the methodology applied.

Chapter 4: presents results obtained after using clinoptilolite as the catalyst support.

Analysis of the data revealed some useful information that can be potentially utilized to reduce capital cost (associated with purchasing of commercial supports).

Chapter 5 which completes the thesis, presents the main conclusions drawn from the work described in this thesis, and offers suggestions for future work.

This dissertation thus provides invaluable information relating to use of natural zeolite in Fischer Tropsch synthesis. The usefulness of this is towards developing best strategies for effective FT runs and performance optimisation. Recommendations for future work are included in the same chapter. Lastly, the list of referenced material is given.

References

[1] J. Baltrusaitis, W.L. Luyben, Sustain. Chem. Eng. 3 (2015) 2100–2111.

[2] M. Williams, Velocys (2014).

[3] G. Aranda, A. Van Der Drift, R. Smit, Ecn-E--14-008 (2014).

[4] H. Veringa, ECN Publ. (2004) 1–24.

[5] R. Sadegh-Vaziri, M. Amovic, R. Ljunggren, K. Engvall, Energies 8 (2015) 5287–5302.

[6] J. Paterson, M. Peacock, E. Ferguson, M. Ojeda, J. Clarkson, Appl. Catal. A Gen. 546 (2017) 103–110.

[7] J. Paterson, M. Peacock, E. Ferguson, M. Ojeda, J. Clarkson, Appl. Catal. A Gen. 546 (2017) 103–110.

[8] D.A. Wood, C. Nwaoha, B.F. Towler, J. Nat. Gas Sci. Eng. 9 (2012) 196–208.

[9] Z. Sihe, Production of Transportation Fuel Range Middle Distillates via Fischer-Tropsch Synthesis with Integrated Product Upgrading under Supercritical Phase Conditions, 2013.

[10] J.A. Velasco, L. Lopez, M. Velásquez, M. Boutonnet, S. Cabrera, S. Järås, J. Nat. Gas Sci. Eng. 2 (2010) 222–228.

[11] R.L. Espinoza, A.P. Steynberg, B. Jager, A.C. Vosloo, Appl. Catal. A Gen. 186 (1999) 13–26.

[12] L.P. Dancuart, A.P. Steynberg, Stud. Surf. Sci. Catal. 163 (2007) 379–399.

[13] J.J.H.M. Font Freide, J.P. Collins, B. Nay, C. Sharp, A History of the BP Fischer-Tropsch Catalyst from Laboratory to Full Scale Demonstration in Alaska and beyond, Elsevier B.V., 2007.

[14] Z. Urban, Chem. Eng. Technol. 39 (2016) 2142–2150.

[15] M.E. DRY, Catal. Today 71 (2002) 227–241.

[16] B. Bao, M.M. El-Halwagi, N.O. Elbashir, Fuel Process. Technol. 91 (2010) 703–713.

[17] F. Pardo-tarifa, Cobalt Catalyst Supports for Fischer-Tropsch Synthesis, 2017.

[18] J. Gorimbo, Catal. Sci. Technol. (2018) 2022–2029.

[19] F.E.M. Farias, F.A.N. Fernandes, F.G. Sales, Lat. Am. Appl. Res. 40 (2010) 161–166.

[20] H. Atashi, S. Razmjooei, M. Khorashadizadeh, M. Shiva, F.F. Tabrizi, S.A.H.S. Mousavi, J. Taiwan Inst. Chem. Eng. 54 (2015) 83–90.

[21] H. Atashi, S. Razmjooei, M. Khorashadizadeh, M. Shiva, F.F. Tabrizi, S.A.H.S. Mousavi, J. Taiwan Inst. Chem. Eng. 54 (2015) 83–90.

[22] P.A. Frey, G.H. Reed, ACS Chem. Biol. 7 (2012) 1477–1481.

[23] M. Rafati, L. Wang, A. Shahbazi, J. CO2 Util. 12 (2015) 34–42.

[24] K. Keyvanloo, B. Huang, T. Okeson, H. Hamdeh, W. Hecker, Catalysts 8 (2018) 77.

[25] P.A. Chernavskii, V.O. Kazak, G.V. Pankina, V.V. Ordomsky, A.Y. Khodakov, ChemCatChem 8 (2016) 390–395.

[26] J. Zhang, J. Chen, J. Ren, Y. Li, Y. Sun, Fuel 82 (2003) 581–586.

[27] S. Bagheri, N.M. Julkapli, S. Bee, A. Hamid, Sci. World J. 2014 (2014).

[28] M.J. Ledoux, C. Pham-huu, Featur. Lab. Des Matériaux, Surfaces Procédés Pour La Catal. ECPM 5 (2001).

[29] G. Jacobs, T.K. Das, Y. Zhang, J. Li, G. Racoillet, B.H. Davis, 233 (2002) 263–281.

[30] R.J. Davis, 216 (2003) 396–405.

[31] R.J. Davis, J. Catal. 216 (2003) 396–405.

[32] A. Kristiani, S. Sudiyarmanto, F. Aulia, L.N. Hidayati, H. Abimanyu, 1001 (2017).

[33] H. Guerra-Nunez, Maria M. J Ramirez, L.A. Santis, Int. J. Adv. Res. 5 (2013) 2423–2430.

[34] J. Gorimbo, B. Taenzana, K. Kapanji, L.L. Jewell, South Africa J. Sci. 110 (2014) 1–7.

[35] P.P. Diale, E. Muzenda, J. Zimba, II (2011).

[36] J. Gorimbo, Effect of the Homoionic Form of Clinoptilolite on Ni2+ Adosorption Isotherms: A Thermodynamic Study, 2011.

[37] B. JHA, D.N. Singh, in:, Fly Ash Zeolites, Adv. Struct. Mater., 2016, pp. 5–31.

[38] J. Gorimbo, X. Lu, X. Liu, D. Hildebrandt, D. Glasser, Appl. Catal. A Gen. 534 (2017) 1–11.

CHAPTER 2

LITERATURE REVIEW

2.1 Introduction

Clinoptilolite is a natural zeolite comprising of a microporous arrangement of silica and alumina tetrahedra. South Africa is endowed with natural zeolite and this review will incorporate most of the valuable available literature on supports paying particular attention to clinoptilolite. Existing supports for different catalyst will be viewed in comparison with the local clinotilolite. Clinoptilolite mined in KwaZulu-Natal, South Africa, was evaluated and based on the chemical composition of the natural clinoptilolite, the molecular formula for the natural zeolite was: $(Na_{1.25}K_{1.6})(Ca_{0.49}Mg_{0.43})(Al_{5.14}Fe_{0.31})(Si_{25.67}Ti_{0.04})O_{62}$[1] (Of which the composition varying with location).

2.2 Support materials

Porous materials such as metal organic framework (MOFs), zeolites (synthetic and natural), porous carbons (activated carbons), clay, porous composites and others have found application in gas storage (hydrogen, methane and carbon dioxide), heat storage electrochemical energy applications, catalysis and other related applications[2] [3][4][5,6]. Based on pore size, zeolite materials are microporous (<2 nm), mesoporous (2−50 nm), and macroporous (>50 nm), thus making them trimodal porous materials[7], i.e. materials that have all three levels of pores.

Catalyst support plays an important role for supported metal catalysts in bringing out the capability of the supported metal as a catalytically active center. Generally, materials for catalyst supports show high surface area, high porosity (average pore size and pore radius distribution), chemical inertness, as well as excellent mechanical properties (attrition resistance, flow resistance in packed bed and stability under reaction conditions) [6,8]. In addition, the capability for highly dispersing metal particles over the surface is also of importance. The aforementioned properties govern the choice of supports to be used in

FTS. For instance, from the tabulated results in **Table 2.1**, carbon based support possesses both high surface area and pore volume. But the carbon based support cannot be in other reactions as the materials used have a weak oxidation resistance to carbon as a support - this hinders its use for high-temperature oxidative reactions [9].

Table 2.1: Typical properties of supports used in Fisher Tropsch synthesis.

Catalyst Support	Surface area (m^2/g)	Pore Volume (cm^3/g)	Average pore radius (nm)	Ref
Silicon carbide (SiC)	30	-	-	[10]
Silica (SiO_2)	192 - 311	0.857 - 1.135	8.9 – 11.5	[11]
Titania, TiO_2	45- 340	-	-	[8]
Alumina (Al_2O_3)	153 -256	0.4 – 0.8	9.6 – 19.0	[12]
Activated carbon	1000−3500	0.6−2	-	[13]
Carbon Nanofibers	137−194	0.21−0.38	30	[6]
Carbon Nanotubes	120−500	2.5	-	[13]
South African Clinoptilolite	13.54 - 16.49	3.11 – 3.79	-	[1]
Al_2O_3	211	0.500	4.7	[14]
15% Co/Al_2O_3	158	0.328	4.2	[14]

Table 2.1 depicts some of the features considered when choosing a support, such as porosity and surface area.

The objective of adding a support is to proffer a large surface area for the formation and stabilization of small metal crystallites in the catalyst. Generally, materials for catalyst supports show high surface area, chemical stability as well as capability for dispersing metal particles highly over the surface. Moreover, the chemical and physical properties of support surfaces affect the activation of supported metals and the long term activity of the catalyst, due to strong metal-support interactions the support may also have major effects on the catalyst activity and selectivity [15]. In fact the chemical nature of the support, its texture and surface acidity can influence metal dispersion, properties of reduction, as well as the interaction between metal and support[16]. Zeolites compounds which are mixed SiO_2–Al_2O_3–TiO_2 oxides, such as clinoptilolite, are promising candidates for catalyst supports if they satisfy the conditions as catalyst supports.

From the literature, several types of catalyst support have been reported and include organic polymers, carbon, dendrimer and mesoporous oxides [13,16–18]. Conventional supports such as alumina, silica and titania are the most industrially used for cobalt and iron based FT catalysts [19–24].

2.2.1 **Conventional supports**

In heterogeneous catalysis, metals and metal oxides are traditionally dispersed as nanoscale particles on a support with a large surface area, so as to maximize the number of exposed active sites. Historically, alumina and silica supports have been used for FTS. It is well documented that in both academic research and industrial application that supports such as alumina(Al_2O_3), silica (SiO_2) and titania (TiO_2) are the most used for FT catalysts. The main advantage of these supports is their retention of high surface area after high calcination temperatures (See Table 2.1) although carbon materials proved to have distinguished merits over metal oxides supports, such as high specific surface area (see table 2.1), diverse pore structure, superior chemical inertness, and good recycling characteristics[6,14,15,23–26]. The properties of the support are also an important factor for producing a feasible catalyst. Much work has been done in order to determine the optimal characteristics of the support.

Alumina (Al_2O_3) support

Alpha (α), Beta (β) and gamma (y) are the known different phases of Alumina. Each of these phases posses characterisitcs that determine its application in different processes. y- Alumina (γ-Al_2O_3) is nano alumina and has high purity and excellent dispersion and high specific surface, with resistance to high temperature and inert, high activity. Porous, hence it is a kind of activated alumina and used as catalyst support and adsorbent in Fischer-Tropsch synthesis[29]. The α- Alumina is also known as Nano alumina and is white puffy powder. The specific surface area is low, resistant to high temperature and inert, but it does not belong to activated alumina, and it has almost no catalytic activity. β- Alumina is hexagonal, with lamellar structure and the unit cell contains two alumina spinel based block[29].

Silica (SiO_2) support

Silicon dioxide has been used a great deal of FTS research due to their chemical, physical and thermal properties. Although in most cases there is no significant interaction between the metal and the support, silica has low hydrothermal stability and can break down in the presence of steam to form cobalt-silicate species that are inactive in the FTS [30], [24]. Similar to alumina, silica supports are also often modified, with stabilizers or promoters such as ZrO_2, K, TiO_2, CeO_2, among others or by organic solvents to increase the hydrothermal stability[24]. Also, it has been shown that calcination of the support prior to metal deposition could reduce the metal support interaction[31].

TiO_2 support

Among the known three titania phases which are anatase, rutile and brookite, anatase is frequently utilized as a catalyst support in heterogeneous catalysis due to its comparative high specific surface area (see table 2.1). It is indicated that brookite, anatase, and rutile differ noticeably in their interaction with particles of metals onto their respective surface[21]. The strong metal support interaction is normally shown on brookite and anatase, and the effect is not as significant on rutile. Generally, TiO_2 was found to have a strong metal support interaction. Despite these drawbacks, a number of studies have focused on catalytic reaction with TiO_2 as a support material[30], [32], [11].

2.2.2 **Non-conventional**

Non-conventional supports have been studied in FTS, such as ZrO_2[33], carbon-based supports[15], metallic supports, zeolites, mesoporous oxides, CeO_2 [34] among others.

2.2.3 **Structural characteristics of the studied Clinoptilolite**

Zeolites consist of interconnected aluminosilicate building blocks of AlO_4 and SiO_4 tetrahedral units, which form three-dimensional framework with linked channel systems and well defined micropores. Because of their high degree of open pores and microporous nature, these materials possess very high surface area[4,35–37] and it is possible to find more than 170 different zeolite crystal structures and their crystallographic data from the database of the International Zeolite Association (IZA)[36]. Generally, the following chemical formula is used used to represent zeolites,

$$A_{y/m}^{m+}\left[(SiO_2)_x(AlO^{-2})_y\right]zH_2O$$

where A is charge-balancing cation with valance m, (x + y) is the number of tetrahedral units per crystallographic unit cell, x/y is the ratio of silicon to aluminum and z is the number of water molecules associated with the zeolite unit cell[36]. The ratio x/y usually varies from 1 to 5 although pure silica form of zeolite is also available with x/y being infinite[38].

Table 2.3: Chemical Composition (Wt. %) of treated Clinoptilolite sample South Africa[1] and Austria[35].

Composition	SiO_2	Al_2O_3	FeO_3	FeO	MnO	MgO	CaO	Na_2O	K_2O	TiO_2	P_2O_5	ref
Wt. (%)	69.05	11.97	0.12	0.99	0.01	*0.68*	0.74	2.75	2.8	0.12	0.02	[1]
Wt. (%)	67.25	11.91	1.43	-	-	*1.01*	2.68	0.76	2.83	-	-	[35]

South African zeolite (Clinoptilolite) consists of all the support commonly used in FTS. These different supports are found to be in different proportions (SiO_2, Al_2O_3 and TiO_2)

and have a variety of promoters (Na_2O, K_2O, MnO and MgO), including FTS active metals that are contained in the natural zeolite (Table 2). Effective reduction of the active phase plays an important role in optimizing catalyst performance, while the addition of small quantities of promoters during the formulation of the catalyst have been found to significantly enhance the reducibility of Co and Fe.

2.2.4 **Synthetic zeolites**

These zeolites are synthesized by chemical processes, which result in a more uniform and purer state as compared to the natural types in terms of their lattice structures, sizes of pores and cages in their frameworks. The principal raw materials useful for synthesis of synthetic zeolites can be pure chemicals rich in silica and alumina, minerals available on the earth or by-products of industries[37]. Fly ash being an abundantly and cheaply available industrial by-product, rich in minerals containing silica and alumina can be an alternative material for synthesis of synthetic zeolites[39–42]. The type of zeolites formed is a function of the temperature, pressure, concentration of the reagent solutions, pH, process of activation and ageing period, SiO_2 and Al_2O_3 contents of the raw materials[36,43,44]. For instance, ZSM-5 (Zeolites Socony Mobil-5) is a synthetic zeolite which contains silica (Si) and alumina (Al) with the ratio of silica greater than the alumina[44]. The name ZSM-5 is because it has a pore diameter of 5 Å (angstroms) and it has more than five Si/Al ratios. The disadvantages of opting for synthetic zeolite is that production cost is high and a complex production process which is highly influenced by time and temperature used[45]. Based on these facts, it is worthwhile to consider alternative natural occuring zeolites.

Metal oxides have been used favourably as promoters for cobalt catalysts such as alkali metal oxides, early and late transition metals, noble metals, as well as lanthanide and actinide series oxides [24]. These are used because they may control the surface H/CO ratio through electronic interaction with the metal, increase and facilitate CO dissociation at the promoter-metal interface, and/or lower support acidity, i.e. preventing side reactions [24].

Effect of adding manganese (Mn)

Manganese (Mn), though found in small quantities, has been reported to improve dispersion of cobalt active phases and also enhances both the carbon monoxide conversion rate and hydrocarbon selectivity [46]. In the case of an iron based catalyst, the presence of manganese retards the reduction of iron in a variety of preparations of mixed iron, i.e. Manganese oxide [47]. Manganese is also found to be beneficial to the catalyst activity and olefin selectivity of iron-based FT catalyst. It is also reported to suppress methane formation and to assist activity loss resistance [48], [49].

Effect of adding phosphorous (P)

Iqbal et al. (2016) [50] have indicated in their studies that the addition of phosphorus to a CoMnOx FT catalyst increases its selectivity to alkenes, particularly propene and butene. Further increases of phosphorous content beyond 0.05 wt% decreased the selectivity to alkenes and increased the CH_4 selectivity [50]. The weight percentage from Table 2 is within the beneficial range of 0.02. The effect of phosphorus on the activity and stability of supported cobalt catalysts for FTS was recently studied by Martinelliet al. (2018) [51]. The study showed completely different effects depending on the support used. For instance, when P is added to Co/Al_2O_3, CO conversion on a per gram catalyst basis decreased, while methane selectivity increased. When SiO_2 is used to support cobalt particles, CO conversion increased. This also resulted in improved catalyst stability during FT testing [51].

Effect of adding sodium (Na)

The use of NaO as a promoter in FT was investigated using carbon-supported iron catalysts. Higher activity and slower loss of activity was observed at low promoter contents (1–3 wt% of sodium) [52]. Sodium contents of 15–30 wt% reportedly led to a rapid loss of catalytic activity due to the covering of the iron surface with promoters during particle growth under FTS operation [52]. Additionally, different promotor sources have also been investigated (Na, NaOH, NaSH, Na_2O and Na_2S) [53] using supported iron FT catalyst.

Effect of adding potassium (K)

The effect of potassium in Fischer Tropsch synthesis was studied by Raje et al, (1998)[54] and the observations were that the FTS activity decreases with potassium loading at low syngas conversions and activity enhanced at high synthesis gas conversions. Also, the promotion with copper and potassium has been shown to enhance iron dispersion and activation of the calcined catalysts in carbon monoxide or syngas results in the reduction of hematite to magnetite at 250–300 °C [55]. In a different study, the addition of the potassium species to nickel catalysts (with various amounts of alkali promoters (1–4 wt% of K_2O),) increases their resistance to coking during hydrocarbon steam reforming[56].

Effect of adding calcium (Ca)

Tao et al. (2006) [57] studied the effect of calcium promoter on a precipitated iron–manganese catalyst for FTS and they found that: (i) calcium promoter has a negligible effect on the textural properties, (ii) calcium promoter enhances the surface basicity of the catalyst, (iii) an appropriate amount of calcium promoter can promote the reduction and carburization of the catalysts, (iv) excessive addition of calcium promoter will decrease the extent of reduction and carburization, (v) the activities of both FTS and water-gas shift (WGS) decrease with the incorporation of calcium promoter and (vi) calcium promoter can inhibit the hydrogenation ability, suppress the formation of methane and enhance the selectivities to olefin and higher molecular weight products. Furthermore, the incorporation of calcium promoter into the iron based catalyst has been shown to promote CO adsorption, increase the concentration of CO species and shift WGS reaction forward - thus improving WGS activity [58].

2.3 Natural versus synthetic supports

Limited studies have focused on the effect of zeolite support on the overall FTS. Amongst these, only the synthetic ones are commercially available and well-studied [8]. Some low-cost supports are superior - including treated carbon, carbons developed from agricultural waste and natural zeolites. A drawback of carbon-based supports is that they are less stable as they can gasify in the presence of hydrogen [59]. Hence, it is important to further study the natural zeolite supported iron FT catalysts.

It is known that there is still controversy about the FT process when it comes to certain features such as mechanism, kinetics, catalyst deactivation and equilibrium. But many researchers have agreed that the main problem with all of the anything-to-liquids (XTL) technologies is that the capital and operational costs are extremely high [60–64]. As a result, securing a cheap feedstock supply and developing a cheap catalyst can also reduce the capital costs of the whole hydrocarbon synthesis. The focus of this work is to experimentally explore the behaviour of the Clinoptilolite (natural zeolite) as catalyst support in FT synthesis.

2.4 Catalyst preparation

Incipient wetness impregnation is the mostly used technique by researchers in preparing supported catalysts in Fischer Tropsch (FT)[66–75]. It is based on filling the pore volume of the support with the appropriate concentration of the metal salt solution. The impregnation step is followed by drying, calcining (see Figure 2.1) in order to decompose the nitrate and obtain supported metal oxide[72–74]. The idea is that the main catalyst should be dispersed on a suitable support to make the catalytic particles stable and obtain optimal performance. In situ reduction transforms the inactive metal oxide to active metallic state prior to Fischer-Tropsch synthesis. This speciation during reduction from metal oxide to metallic metal is shown to be thermodynamics feasible for iron catalyst by Gorimbo et al, (2017)[75].

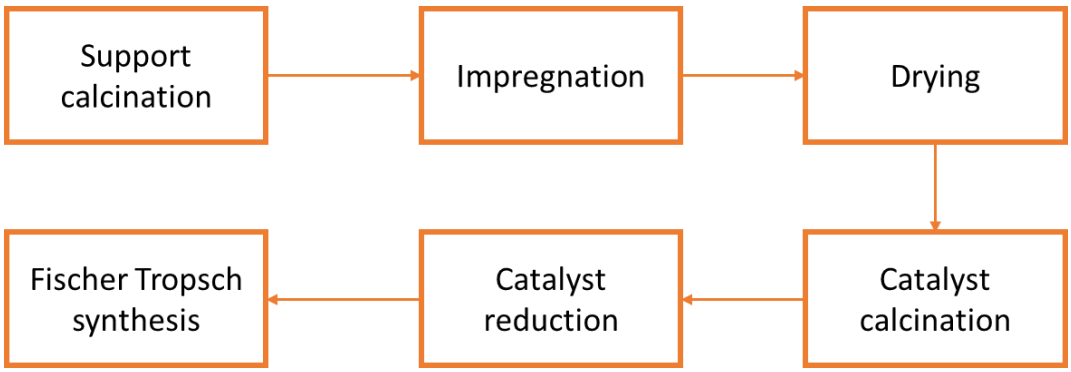


Figure 2.1: Catalyst preparation steps.

Each of these steps needs to be optimized in order to prepare a catalyst with high activity and dispersion. The conditions during calcination of the deposited metal have a significant influence on the physicochemical characteristics of the final catalyst.

2.5 Catalyst pre-treatment

The catalysts, synthesized in the form of a metal oxide, are subjected to an activation treatment prior to FT synthesis. Iron and Cobalt are commonly reduced in H_2 at temperatures between 200 to 400 ^oC depending on the H_2-TPR profiles of catalyst. In some instances, researchers use carbon monoxide (CO) or synthesis gas (CO, H_2) to reduce iron based catalyst in-situ. Before reduction, the metal is present in the oxide form and a two or three-step reduction depending on the oxide is observed (see example of a H_2-TPR profile **Figure 2.2**).

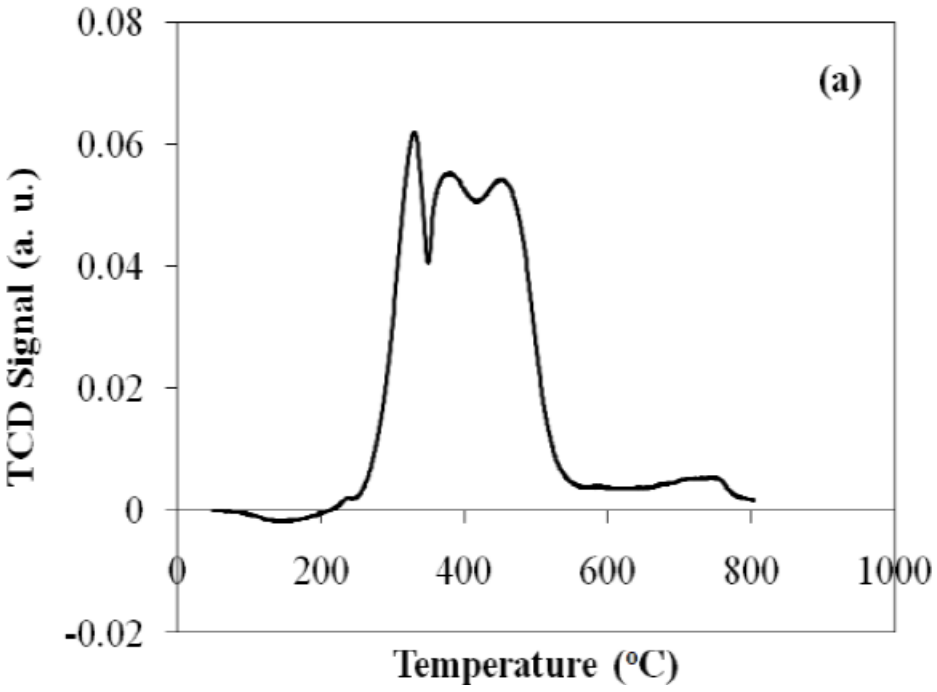


Figure 2.2: Typical TPR profiles for the calcined and unreduced catalysts 10% Co/TiO_2[76] (Co_3O_4 to Co).

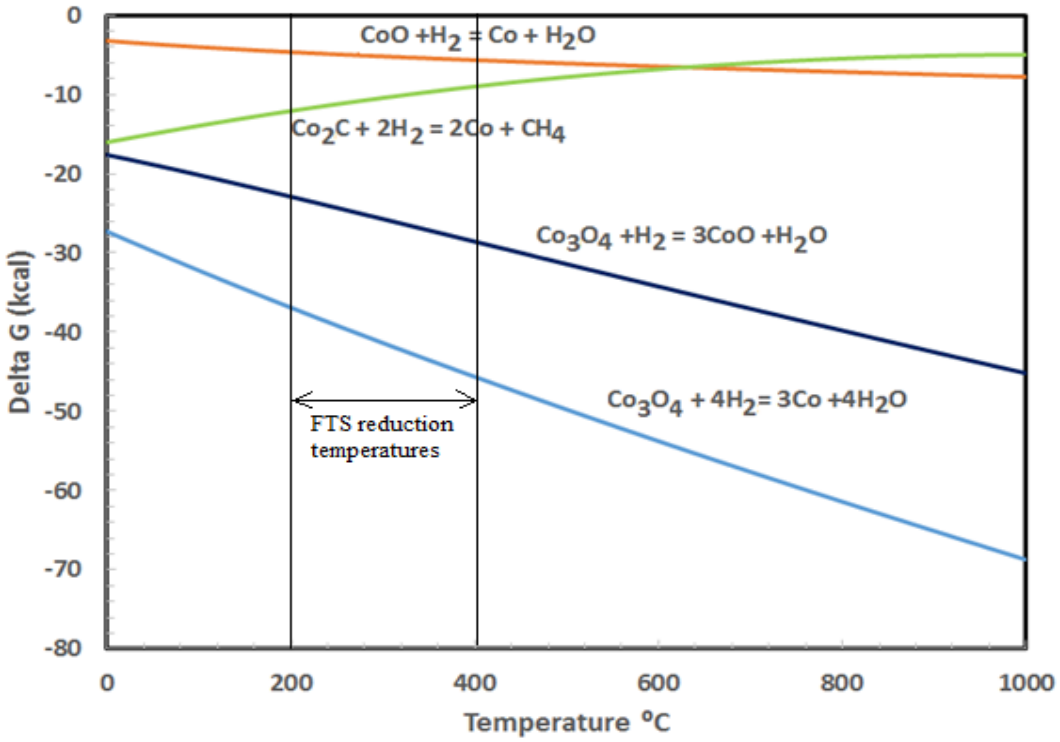


Figure 2.3: FTS reduction temperatures for cobalt based catalyst.

The catalyst precursor is often in the form of cobalt oxide spinel (Co_3O_4) on a support, and this undergoes reduction treatments to reach the active catalyst (Co) (see figure 2.3), all of which is inside the reactor and not observed or measured by an operator. Initial analysis to ascertain a successful transformation from Co_3O_4 to metallic Co is done using H_2-TPR. Overall reaction is:

$$H_2\ reduction \qquad Co_3O_4 + 4H_2 \rightarrow 3Co + 4H_2O \qquad \text{equation 2.1}$$

For any given loading of cobalt on the catalyst, 1 mol of Co_3O_4 spinel will produce 4 mol of water during reduction.

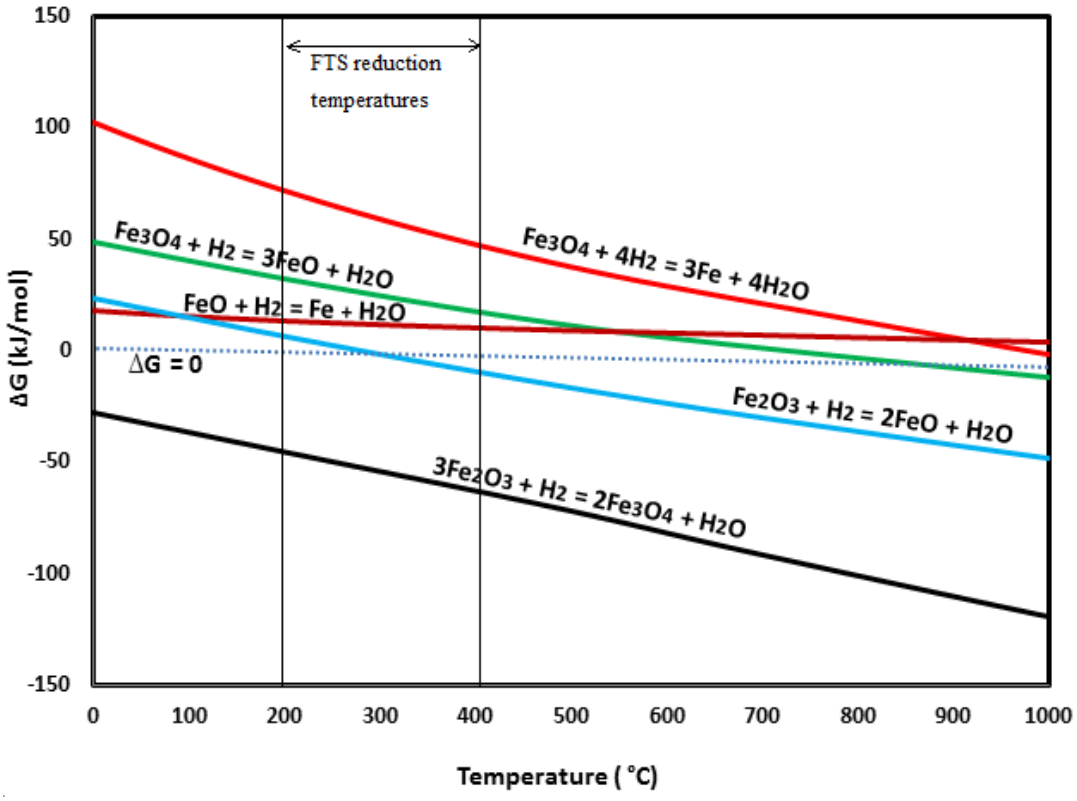


Figure 2.4: FTS reduction temperatures for Iron based catalyst[75].

Activation of Fe_2O_3 with H_2 is known to take a two-stage reduction step with metallic iron as the final product. For every mole of hydrogen consumed, a mole of H_2O is produced (see figure 2.4).

$3Fe_2O_3 + H_2 \rightarrow 2Fe_3O_4 + H_2O$ equation 2.2

$Fe_3O_4 + 4H_2 \rightarrow 3Fe + 4H_2O$ equation 2.3

2.6 Iron Based Fischer-Tropsch Catalyst

Iron based FT catalyst is comparatively cheaper than cobalt based catalyst. Iron based catalysts tend to produce products with higher olefinic concentration[77]. Iron based catalysts can be primarily separated into two types: fused iron based [78,79] catalysts for HTFT and precipitated iron based catalysts for LTFT, further into two types: supported and unsupported (or self-supported). The precipitated iron based catalyst used in the Slurry Bed

Reactor process is similar to that used in the TFBR (ARGE reactors) [80–82], except that the sizes are different (one is power and one is pellet, respectively)[62].

Though iron catalysts are usually self-supported, supports such as SiO_2, are also frequently added to improve thermal and mechanical stability[62],[83]. Silica is generally accepted as one of the best supports.

2.7 Thermal conductivity

Thermal conductivity of catalyst support materials used in Fischer Tropsch synthesis plays a critical role in determining how well the material will intrinsically dissipate heat through the catalyst bed to improve heat transfer in fixed bed reactors. Fisher Tropsch synthesis is highly exothermic, it is known to produce $\Delta H = -165\ kJ/mol_{co}$ consumed, which dramatically raises catalyst bed temperature beyond the allowed limit [84]. This leads to development of thermal hotspot in catalyst bed and consequently deactivates the catalyst by thermal sintering. So, using thermally conductive support material dissipates heat of reaction and helps to control catalyst bed temperature [85]. For most catalyst support materials, conductivity decreases as the temperature increases before phase transition of the material. Other parameters, beside the temperature, such as density and porosity of the material have influence on thermal conductivity of the catalyst support material [86].

The following table shows conductivity as a function of temperature for selected catalyst support materials.

Table 2.4: Variation of thermal conductivity of selected support materials with temperature [87].

	Alumina	Magnesium oxide	Silica single crystal parallel to axis	Silica single crystal perpendicular to axis	Titanium oxide
Temperature	Conductivity	Conductivity	Conductivity	Conductivity	Conductivity
K	w/mk	w/mk	w/mk	w/mk	w/mk
40			1.79	0.89	
60			0.85	0.429	
80			0.54	0.279	
100	1.33		0.39	0.208	
150	0.77		0.231	0.130	
200	0.55		0.164	0.095	
250	0.434	0.580	0.127	0.075	0.093
273	0.397	0.531	0.116	0.0684	0.089
300	0.360	0.484	0.104	0.0621	0.084
350	0.307	0.412	0.088	0.0530	0.0767
400	0.264	0.356	0.076	0.0470	0.0701
500	0.202	0.269	0.060	0.0388	0.0588
600	0.158	0.207	0.050	0.0340	0.0502
700	0.126	0.165	0.0447	0.0314	0.0439
800	0.104	0.134	0.0420	0.0306	0.0394
900	0.089	0.112			0.0365

1000	0.0785	0.097			0.0346
1100	0.0710	0.085			0.0335
1200	0.0655	0.077			0.0328
1300	0.0613	0.072			0.0323
1400	0.0585	0.068			0.0321
1500	0.0566	0.065			
1600	0.0556	0.064			
1700	0.0554	0.066			
1800	0.0559	0.074			
1900	0.0574	0.085			
2000	0.0600	0.099			
2100	0.0644	0.115			

Table 2.5: Thermal conductivities of different catalyst supports for Fischer Tropsch synthesis at different temperatures and densities

Support material	Thermal conductivity (W/mK)	Density (kg/m^3)	Temperature (K)	Reference
Natural supports				
• Carbon supports				
○ CNTs, CNTs materials	3000- 3500	-	273	[88]
	10- 220		273	[89]
○ Carbon foams				
• Fly ash				
• Zeolite	1.254	-	623	[40]
○ ZSM- 5				
○ Na- X	3.63		423	[90]
	0.185	-	400	[39]
Synthetic supports				
• Silicon Carbide	106.0	3210		[85]
• Silica	1.58, 1.63	-	450, 500	[91]
• Alumina				
○ $\propto$ −Alumina	30	-	293	[92]

The poor heat conductivity and the chemical reactivity of alumina and silica can induce a decrease in surface area and loss of active phase during operation. Another important property of the support is its mechanical strength. In large industrial reactors, the collapse of the structure (catalyst bed) under its own weight should obviously be avoided because it will result in a severe and not easily corrected pressure drop.

2.8 Anderson-Schulz-Flory Model

The overall reaction rate and product distribution are affected by various physical and chemical processes including:

- diffusion of reactants into and inside a porous particle to active site
- adsorption of reactants on active sites
- chain initiation
- chain growth
- chain termination
- product desorption
- re-adsorption with further reaction
- diffusion of products towards the outside of the particle

To determine the mechanism of FT reactions, the selectivity data is important. Flory was the first to investigate the synthetic behavior of non-homogenous material given the polymerization nature of the FT process, proposing the first FTS chain-growth model. A series of studies afterwards led to the current well known Anderson-Shultz-Flory (ASF) product distribution model (Herrington1946, Anderson 1950, Henrici-Olive 1976). The polymerization reaction starts from the formation of an initiator. The first major assumption is that the chain growth is by addition of one monomer at a time. The second

major assumption is that the growth and termination rates are independent of the chain length, yielding the chain growth probability (α) as following:

$$\alpha = \frac{rp_i}{(rp_i)+rt_i} = \frac{\sum_{i+1}^{n} N_i}{\sum_{i}^{n} N_i} \qquad \text{equation 2.4}$$

$$\alpha = \frac{N_{i+1}}{N_i} = \frac{R_P}{R_P+R_t} \qquad \text{equation 2.5}$$

Where R_p and R_t are the propagation rate and termination rate, respectively. rp_i and rt_i are the propagation rate and termination rate for a hydrocarbon (or oxygenated hydrocarbon) with i as the carbon number in the carbon chain. N is the molar rate (concentration) of product on the surface of the catalyst, and i is the carbon number of the carbon chain. n is the biggest number the carbon number can achieve in the reaction for hydrocarbons. The weight fraction of a chain of length i, W_i, can be measured as a function of the chain growth probability.

$$W_i = i\alpha^{i-1}(1-\alpha) \qquad \text{equation 2.6}$$

Which rearranges to:

$$\frac{W_i}{i} = (\alpha^{i-1})(1-\alpha) \qquad \text{equation 2.7}$$

The logarithmic relation is as follows:

$$\ln\left(\frac{W_i}{i}\right) = i\ln\alpha + \ln\left(\frac{(1-\alpha)}{\alpha}\right) \qquad \text{equation 2.8}$$

According to the ASF assumptions, the plot of $\ln\left(\frac{W_i}{i}\right) vs\ i$ should be a straight line for all hydro carbon products, and α can be determined from the slope of this straight line. According to these equations, heavier hydrocarbons are produced as α increases[48]. There are also reported data showing deviation from ASF behaviour, which has been demonstrated as possessing two distinct reaction pathways with different chain growth factor α[93], [94]. Extensions of the ideal Anderson–Schulz–Flory (ASF) distribution were considered for Fischer–Tropsch reactions products to account for experimentally observed

deviations[95]. The quasi-ASF plots were developed and applied by Tavakoli et al (2007)[96] for systems that can not be described by the ASF equation. A quasi-ASF plots follow the same trends as those of ASF but with an improved linearity.

The majority of the reported ASF plots showed a nearly straight line only in the $C_4 - C_{12}$ region[97], [95]. A number of authors have determined the growth factor from the straight-line portion of the ASF plot[98][97][99][100].

2.9 Yao plots

A plethora of models have been developed in the past in an endeavour to describe the distribution of the products obtained in FT processes. Yao plots just like the ASF has been used previously by a researcher belonging to the Institute for the Development of Energy for African Sustainability (IDEAS) [76,101] to explain the product distribution; however, some significant deviations from this ideal distribution have been observed. These deviations are observed regardless of the nature of the catalyst; both iron and cobalt catalysts have showed this deviation.

Yao plots are based on quasi reaction equilibrium, which are developed to explain the linear relationship between $P_{(n+1)}/O_{(n+1)}$ and $P_{(n)}/O_{(n)}$. The plot assumes that the reaction of $C_{n+1}H_{2n+2}+C_nH_{2n+2}=C_{n+1}H_{2n+4}+C_nH_{2n}$ reaches quasi-equilibrium. A simple vapour-liquid equilibrium (VLE) model indicates that the ratio of $P_{(n+1)}/O_{(n+1)}$ to $P_{(n)}/O_{(n)}$ changes in a range of (1, 1/β), where β is the variation of the vapour pressure coefficient. Experimental results support the expression very well when the chain length is n>2. But with chain length n=2[76]. The relationship between $P_{(n+1)}/O_{(n+1)}$ and $P_{(n)}/O_{(n)}$ is shown in **equation 2.9** for n>2 and **equation 2.10** for n=2.

$$\left.\frac{P_{(n+1)}/O_{(n+1)}}{P_{(n)}/O_{(n)}}\right|_{n>2} \approx \xi_{n>2} \qquad \text{equation 2.9}$$

$$\left.\frac{P_{(3)}/O_{(3)}}{P_{(2)}/O_{(2)}}\right|_{n=2} \approx \xi_{n=2} \qquad \text{equation 2.10}$$

For n > 2, the ξ values take any number greater than zero (**see Figure 2.5**).

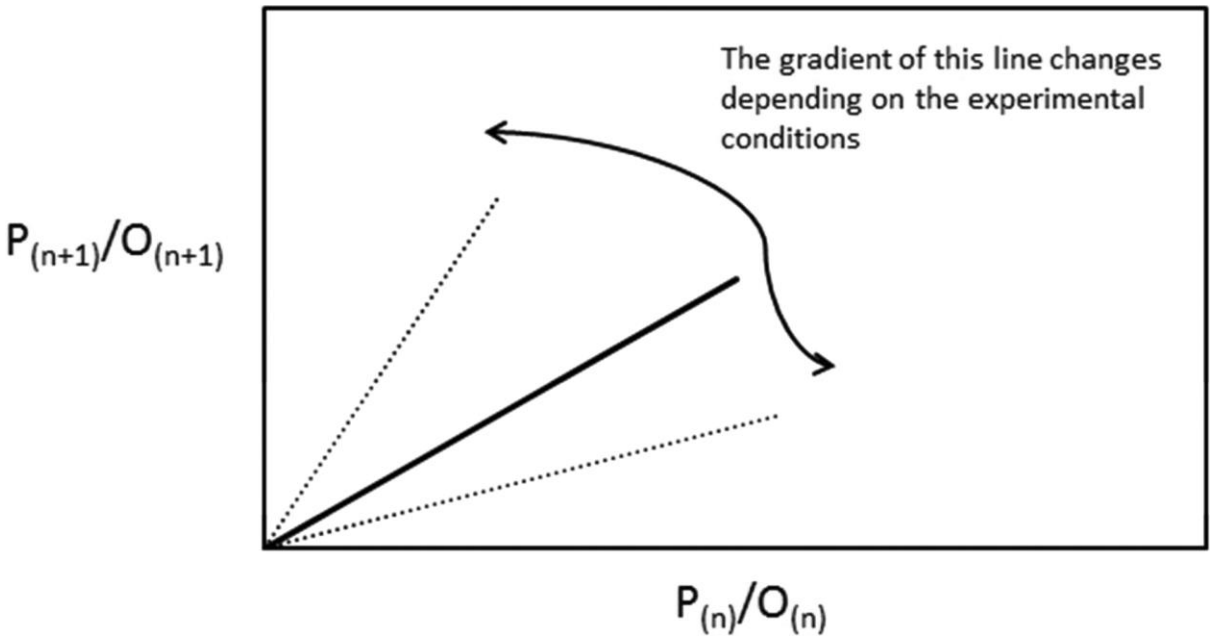


Figure 2.5: Plot of the ratio of P(n + 1)/O(n + 1) as a function of the ratio of Pn/On for FTS[101].

In the Yao plots, two simple models are developed: one based on the assumption of vapor−liquid equilibrium (VLE) and the other is based on quasi-reaction equilibrium to explain unique experimental observation[102]. This model tends to indicate that the olefin and paraffin distributions are not independent.

References

[1] J. Gorimbo, B. Taenzana, K. Kapanji, L.L. Jewell, South Africa J. Sci. 110 (2014) 1–7.

[2] S. Biollaz, T. Schildhauer, J. Held, R. Seiser, Tcbiomass 2015, Int. Conf. Thermochem. Convers. Sci. (2015).

[3] O. Rubric, (n.d.).

[4] R.J. Davis, 216 (2003) 396–405.

[5] M. Zaman, A. Khodadi, Y. Mortazavi, Fuel Process. Technol. 90 (2009) 1214–1219.

[6] H. Xiong, L.L. Jewell, N.J. Coville, ACS Catal. 5 (2015) 2640–2658.

[7] H. Funabashi, S. Takeuchi, S. Tsujimura, Sci. Rep. (2017) 1–9.

[8] J.M. González Carballo, E. Finocchio, S. García, S. Rojas, M. Ojeda, G. Busca, J.L.G. Fierro, Catal. Sci. Technol. 1 (2011) 1013–1023.

[9] M.J. Ledoux, C. Pham-huu, Featur. Lab. Des Matériaux, Surfaces Procédés Pour La Catal. ECPM 5 (2001).

[10] M. Lacroix, L. Dreibine, B. De Tymowski, F. Vigneron, D. Edouard, D. Bégin, P. Nguyen, C. Pham, S. Savin-poncet, F. Luck, M. Ledoux, C. Pham-huu, "Applied Catal. A, Gen. 397 (2011) 62–72.

[11] G. Jacobs, T.K. Das, Y. Zhang, J. Li, G. Racoillet, B.H. Davis, 233 (2002) 263–281.

[12] J. Zhang, J. Chen, J. Ren, Y. Li, Y. Sun, Fuel 82 (2003) 581–586.

[13] E. Lam, J.H.T. Luong, ACS Catal. 4 (2014) 3393–3410.

[14] G. Jacobs, P.M. Patterson, Y. Zhang, T. Das, J. Li, B.H. Davis, Appl. Catal. A 233 (2002) 215–226.

[15] M.R.M. Abbaslou, Iron Catalyst Supported on Carbon Nanotubes for Fischer-Tropsch Synthesis : Experimental and Kinetic Study, 2010.

[16] B. Sun, K. Xu, L. Nguyen, M. Qiao, F. Feng, ChemCatChem 4 (2012) 1498–1511.

[17] H. Xiong, L.L. Jewell, N.J. Coville, (2015).

[18] N.M. Julkapli, S. Bagheri, Int. J. Hydrogen Energy 40 (2014) 948–979.

[19] H. Al-Megren, H. Chen, Y. Huang, M. AlKinany, P.P. Edwards, T. Xiao, Y. Wang, Appl. Petrochemical Res. 3 (2013) 25–34.

[20] M. Trueba, S.P. Trasatti, Eur. J. Inorg. Chem. (2005) 3393–3403.

[21] S. Bagheri, N.M. Julkapli, S. Bee, A. Hamid, Sci. World J. 2014 (2014).

[22] K. Keyvanloo, W.C. Hecker, B.F. Woodfield, C.H. Bartholomew, J. Catal. 319 (2014) 220–231.

[23] T.R. Motjope, T.H. Dlamini, in:, AIP Conf. Proc., 2005, pp. 43–48.

[24] F. Pardo-tarifa, Cobalt Catalyst Supports for Fischer-Tropsch Synthesis, 2017.

[25] M.G.A. Cruz, F.A.N. Fernandes, A.C. Oliveira, J.M. Filho, A.C. Oliveira, A.F. Campos, E. Padron-Hernandez, E. Rodríguez-Castellón, Catal. Today 282 (2017) 174–184.

[26] T. Fu, Z. Li, Chem. Eng. Sci. 135 (2015) 3–20.

[27] N.E. Tsakoumis, R. Dehghan, R.E. Johnsen, A. Voronov, W. Van Beek, J.C. Walmsley, Ø. Borg, E. Rytter, D. Chen, M. Rønning, A. Holmen, 205 (2013) 86–93.

[28] G.L. Bezemer, J.H. Bitter, H.P.C.E. Kuipers, H. Oosterbeek, J.E. Holewijn, X. Xu, F. Kapteijn, A.J. Van Dillen, K.P. De Jong, (2006) 11568–11569.

[29] K.Y. Paranjpe, Pharma Innov. J. 6 (2017) 236–238.

[30] J. van de Loosdrecht, B. Balzhinimaev, J.A. Dalmon, J.W. Niemantsverdriet, S. V. Tsybulya, A.M. Saib, P.J. van Berge, J.L. Visagie, Catal. Today 123 (2007) 293–302.

[31] R. Naumann, M. Friedrich, E. Kunkes, D. Rosenthal, F. Girgsdies, B. Zhang, L. Shao, M. Schuster, M. Behrens, R. Schlögl, J. Catal. J. 317 (2014) 220–228.

[32] J. Paterson, M. Peacock, E. Ferguson, M. Ojeda, J. Clarkson, Appl. Catal. A Gen. 546 (2017) 103–110.

[33] J. Barrientos, Deactivation of Cobalt and Nickel Catalysts in Fischer-Tropsch Synthesis and Methanation, 2016.

[34] L. Wang, H. Liu, Catal. Today 316 (2018) 155–161.

[35] K. Stocker, M. Ellersdorfer, M. Lehner, J.G. Raith, BMH 162 (2017) 142–147.

[36] H. Guerra-Nunez, Maria M. J Ramirez, L.A. Santis, Int. J. Adv. Res. 5 (2013) 2423–2430.

[37] (n.d.).

[38] J. Gorimbo, EFFECT OF THE HOMOIONIC FORM OF CLINOPTILOLITE ON Ni 2 + ADSORPTION ISOTHERMS : A THERMODYNAMIC STUDY, UNiversity of the Witwatersrand, 2011.

[39] B. Jha, D.N. Singh, 78 (2016).

[40] W. Wang, C. Lu, Y. Li, Q. Li, Constr. Build. Mater. 148 (2017) 148–154.

[41] E. Wibowo, M. Rokhmat, R. Murniati, M. Abdullaha, Procedia Eng. 170 (2017) 8–13.

[42] C. Ash, (2011).

[43] T. Properties, S. Zeoiites, (2000).

[44] W. Widayat, N. Annisa, A, in:, IOP Conf. Ser. Mater. Sci. Eng., 2017, pp. 1–8.

[45] (2015).

[46] A.Y. Khodakov, W. Chu, P. Fongarland, Am. Chem. Soc. 107 (2007) 1692–1744.

[47] I.R. Leith, M.G. Howden, Appl. Catal. 37 (1988) 75–92.

[48] Z. Sihe, Production of Transportation Fuel Range Middle Distillates via Fischer-Tropsch Synthesis with Integrated Product Upgrading under Supercritical Phase Conditions, 2013.

[49] W. Warayanon, S. Tungkamani, H. Sukkathanyawat, M. Phongaksorn, T. Ratana, T. Sornchamni, Effect of Manganese Promoter on Cobalt Supported Magnesia Catalyst for Fischer-Tropsch Synthesis, Elsevier B.V., 2015.

[50] S. Iqbal, T.E. Davies, J.S. Hayward, D.J. Morgan, K. Karim, J.K. Bartley, S.H. Taylor, G.J. Hutchings, Catal. Today (2016).

[51] M. Martinelli, K. Gnanamani, S.D. Hopps, D.E. Sparks, ChemCatChem (2018) 3709–3716.

[52] M. Oschatz, N. Krans, J. Xie, K.P. De Jong, J. Energy Chem. 25 (2016) 985–993.

[53] J. Xie, J. Yang, A.I. Dugulan, A. Holmen, D. Chen, K.P. De Jong, M.J. Louwerse, ACS Catal. (2016).

[54] A.P. Raje, R.J. O'Brien, B.H. Davis, J. Catal. 43 (1998) 36–43.

[55] P.A. Chernavskii, V.O. Kazak, G. V Pankina, Y.D. Perfiliev, T. Li, A.Y. Khodakov, Catal. Sci. Technol. (2017) 2325–2334.

[56] K. Stołecki, J. Dmytrzyk, A. Kotarba, Appl. Surf. Sci. 300 (2014) 191–200.

[57] Z. Tao, Y. Yang, C. Zhang, T. Li, J. Wang, H. Wan, H. Xiang, Y. Li, Catal. Commun. 7 (2006) 1061–1066.

[58] Y. Zamani, A. Zamaniyan, F. Bahadoran, M. Shojaei, J. Pet. Sci. Technol. 5 (2015) 21–27.

[59] A.K. Dalai, B.H. Davis, Appl. Catal. A Gen. 348 (2008) 1–15.

[60] M. Ojeda, S. Rojas, Biofuels from Fischer-Tropsch Synthesis, 2012.

[61] K. Aasberg-Petersen, T.S. Christensen, I. Dybkjaer, J. Sehested, M. Østberg, R.M. Coertzen, M.J. Keyser, A.P. Steynberg, in:, Stud. Surf. Sci. Catal., Elsevier, 2004, pp. 258–405.

[62] M.E. Dry, A.P. Steynberg, in:, Stud. Surf. Sci. Catal., 2004, p. 406.

[63] E. van Steen, M. Claeys, Chem. Eng. Technol. 31 (2008) 655–666.

[64] R. Rauch, A. Kiennemann, A. Sauciuc, in:, Role Catal. Sustain. Prod. Bio-Fuels Bio-Chemicals, 2013, pp. 397–443.

[65] J. Yang, E.Z. Tveten, D. Chen, A. Holmen, 228 (2010) 16558–16567.

[66] J.P. Den Breejen, J.R.A. Sietsma, H. Friedrich, J.H. Bitter, K.P. De Jong, 270 (2010) 146–152.

[67] A.A. Muleja, Y. Yao, D. Glasser, D. Hildebrandt, Ind. Eng. Chem. Res. 56 (2017) 469–478.

[68] Y. Zhang, Y. Yoneyama, N. Tsubaki, Am. Chem. Soc. Div. Fuel Chem. 49 (2004) 647–648.

[69] D.B. Bukur, Z. Pan, W. Ma, G. Jacobs, B.H. Davis, Catal. Letters 142 (2012) 1382–1387.

[70] A.A. Muleja, Study of the Selectivity To Light Hydrocarbons in Fischer-Tropsch Synthesis, University of the Witwatersrand, 2016.

[71] M. Rafati, L. Wang, A. Shahbazi, J. CO2 Util. 12 (2015) 34–42.

[72] H. Karaca, J. Hong, P. Fongarland, P. Roussel, A. Griboval-Constant, M. Lacroix, K. Hortmann, O. V. Safonova, A.Y. Khodakov, Chem. Commun. 46 (2010) 788–790.

[73] R. Dehghan, T.W. Hansen, J.B. Wagner, A. Holmen, E. Rytter, Ø. Borg, J.C. Walmsley, (2011) 754–761.

[74] T.K. Das, G. Jacobs, P.M. Patterson, W.A. Conner, J. Li, B.H. Davis, 82 (2003) 805–815.

[75] J. Gorimbo, Catal. Sci. Technol. (2018) 2022–2029.

[76] Y. Yao, Fischer-Tropsch Synthesis Using Co 2 -Containing Syngas Mixtures Over Cobalt and Iron Based Catalysts, Thesis, 2011.

[77] J. Gorimbo, X. Lu, X. Liu, Y. Yao, D. Hildebrandt, D. Glasser, Ind. Eng. Chem. Res. 56 (2017) 4267–4274.

[78] C.N. Satterfield, G. Huff Jr, J. Catal. 197 (1982) 187–197.

[79] D.B. Bukur, L. Nowicki, S.A. Patel, Can. J. Chem. Eng. 74 (1996) 399–404.

[80] R.L. Espinoza, A.P. Steynberg, B. Jager, A.C. Vosloo, Appl. Catal. A Gen. 186 (1999) 13–26.

[81] L.P. Dancuart, A.P. Steynberg, Stud. Surf. Sci. Catal. 163 (2007) 379–399.

[82] M.E. DRY, Catal. Today 71 (2002) 227–241.

[83] M. Argyle, C. Bartholomew, Catalysts 5 (2015) 145–269.

[84] R. Philippe, M. Lacroix, L. Dreibine, C. Pham-Huu, D. Edouard, S. Savin, F. Luck, D. Schweich, Catal. Today 147 (2009).

[85] X. Zhu, X. Lu, X. Liu, D. Hildebrandt, D. Glasser, Chem. Eng. J. 247 (2014) 75–84.

[86] NPTEL, NPTEL – Chem. Eng. – Catal. Sci. Technol. Lect. (2014) 1–53.

[87] R.W. Powell, C.Y. Ho, P.E. Liley, (1966).

[88] A.A. Balandin, Nat. Mater. 10 (2011) 569–581.

[89] A.N. Volkov, L. V. Zhigilei, Appl. Phys. Lett. 101 (2012) 3–7.

[90] T. Shimonosono, Y. Hirata, K. Nishikawa, S. Sameshima, K. Sodeyama, T. Masunaga, Y. Yoshimura, Materials (Basel). 11 (2018) 1–11.

[91] O.A. Sergeev, A.G. Shashkov, A.S. Umanskii, J. Eng. Phys. 43 (1982) 1375–1383.

[92] I. Zake-Tiluga, V. Svinka, R. Svinka, B. Zierath, P. Greil, T. Fey, J. Eur. Ceram. Soc. 36 (2016) 1469–1477.

[93] H.G. Stenger, J. Catal. 92 (1985) 426–428.

[94] G.A. Huff Jr, C.N. Satterfield, J. Catal. 85 (1984) 370–379.

[95] D. Förtsch, K. Pabst, E. Groß-hardt, Chem. Eng. Sci. 138 (2015) 333–346.

[96] A. Tavakoli, M. Sohrabi, A. Kargari, NSTI-Nanotech 4 (2007) 377–380.

[97] B. Todic, T. Olewski, N. Nikacevic, D.B. Bukur, Chem. Eng. Trans. 32 (2013) 793–798.

[98] M.N. Hassankiadeh, A. Haghtalab, Chem. Eng. Commun. 6445 (2013) 1563–5201.

[99] G.A.O. Junhu, W.U. Baoshan, Z. Liping, Y. Yong, H.A.O. Xu, X.U. Yuanyuan, L.I. Yongwang, CHINESE J. Catal. 32 (2011).

[100] A.P. Savost'yanov, G.B. Narochnyi, R.E. Yakovenko, V.G. Bakun, N.D. Zemlyakov, Catal. Ind. 6 (2014) 292–297.

[101] J. Gorimbo, A. Muleja, X. Lu, Y. Yao, X. Liu, D. Hildebrandt, D. Glasser, Energy & Fuels 31 (2017) 5682–5690.

[102] Y. Yao, Fischer-Tropsch Synthesis Using Co 2 -Containing Syngas Mixtures Over Cobalt and Iron Based Catalysts, University of the Witwatersrand, 2011.

CHAPTER 3

EXPERIMENTAL METHODOLOGY

3.1 Introduction

In this chapter, the writer provides descriptive details of the experimental procedures in order to obtain the laboratory-scale results that form the basis of discussion in the subsequent chapters. The first part of this description comprises a brief overview of the material and chemicals such as the natural zeolite support for the FT catalyst and gases. The second part explains how the researcher set up the rig and provides a diagram of the process and the instrumentation, to aid readers to follow the sequence that connects the experimental units. Lastly, the author outlines the procedures required to run the Fischer Tropsch (FT) system, collect the data, and analyse them with gas chromatography instruments.

3.2 Material and chemicals

The natural zeolite (Clinoptilolite) was obtained from Pratley Mining Company, Krugersdrop, South Africa and used as support in the preparation of Fischer-Tropsch catalyst. This enabled the author to investigate and compare the efficiency of clinoptilolite with traditional supports (silicon dioxide, aluminium oxide and titanium dioxide) used industrially in FT process. Iron(III) nitrate nonahydrate ($Fe(NO_3)_3 \bullet 9H_2O$) was used as the iron precursor and it was obtained from Sigma Aldrich.

The gases required for FT synthesis were supplied by African Oxygen (AFROX Ltd), in standard gas cylinders (40 Kg) for use in the laboratory. Synthesis gas ($H_2/CO/N_2$) or syngas used for reduction and reaction had a molar composition of $H_2/CO/N_2$ =60%/30%/10%. Other gases included argon, helium, hydrogen and air (the carrier gases and the auxiliaries) used for gas chromatography (GC) operations and were of ultra-high purity (UHP) grades (> 99.9997%) unless otherwise stated. The online GC was calibrated by means of a special gas mixture comprising H_2, CO, CO_2, N_2, CH_4, C_2H_4, and C_2H_6.

The author also used UHP He and Ar (baseline) gases to calibrate the thermal conductivity detector (TCD), and air instrument grade (AIG zero), H_2 (UHP) and the carrier gas Ar (baseline) for the flame ionization detector (FID) used during the sample analysis with the GC. The cylinders were fitted with pressure regulators, and the gases were sent to the FT rig via high pressure lines. Nitrogen gas was used for leak testing, purging the system and mass balance calculation. The components of the syngas and calibration gases are given in Table 3.1.

Table 3.1: Components and mole percentage of the calibration gases used in the study.

Component	Mole percentage (% mol)	
	Syngas (mole %)	Calibration gas (mole %)
H_2	60	53.2
CO	30	28.8
N_2	10	9.8
CO_2		5.0
CH_4		2.5
C_2H_4		0.2
C_2H_6		0.5

3.2.1 Catalyst preparation

The Clinoptilolite supported iron (Fe/Clino) catalyst was prepared by depositing an iron precursor component onto the clinoptilolite support from the precursor solution using incipient wetness impregnation method as reported in the literature [1,2]. The zeolite (Clinoptilolite) support was first pre-treated by mixing it with distilled water in a mass ratio of

1:1, and air dried at 120 ^{0}C for 1 hour. This was then followed by 16 hours calcinations at 400 ^{0}C. The calcined material was then crushed and sieved resulting in particles with diameters between 0.5–1 mm. Thereafter, the treated support was impregnated with Fe $(NO_3)_3$•$9H_2O$ solution sufficient enough to give an iron metal loading of 10% by mass. After impregnation, the impregnated material was then dried in air at 120 ^{0}C for 16 hours and again calcined in air at 400 ^{0}C for 6 hours. This process allowed the iron nitrate to decompose and transform to iron oxide, as well as removing solvent and/or water therefrom - resulting in the formation of the Fe-Clino catalyst. The most attractive feature of this method of preparation is its simplicity of practical application. The method is also comparatively economical and has been employed by several Fischer Tropsch practitioners [3–5].

3.2.2 **Catalyst characterization**

Characterization, which involves the investigation and measurement of a material in terms of its structure and properties, is critical to understanding the nature of the catalyst that was used in the experiments. The properties, which include its chemical composition, surface area, pore volume and morphology, are in turn responsible for the catalyst's selectivity, and hence affect the distribution of the FT product [6,7]. The researcher used various characterization techniques to determine the physico-chemical characteristics of the iron catalyst. For example, powder X-ray diffraction (XRD) was employed to assess the crystallinity of the iron loaded, and to verify the phases of iron in the catalyst; whereas electron microscopy was used to determine the particle morphology and iron crystallite size. The physicochemical characteristics of catalysts were determined by means of the Brunauer-Emmett-Teller (BET) and X-ray diffraction (XRD) analysis methods. The characterization techniques used in this study were similar to those reported by other researchers[3,8]

Temperature programmed reduction (TPR)

The reducibility of the catalysts was investigated by hydrogen temperature-programmed reduction (TPR). The calcined catalysts were studied in a Micromeritics Autochem ll 2920. 50mg of samples was placed in a quartz U-tube. The sample was flushed with argon while the temperature was increased to 150 °C at a ramping rate of 10 °C/min and held at that temperature for 30 minutes to remove impurities/moisture. The sample was then cooled to

room temperature under flowing argon, the gas was switched to 10%H_2 in argon. The temperature was increased to 950 °C at 10 °C/min ramp rate. The H_2 consumption was monitored using a TCD during the experiment by the difference in thermal conductivity between the inlet and outlet gases.

X-ray Florescence

X-ray florescence (XRF) of the natural clinoptilolite support and 10%Fe/Clino catalyst was performed on a Malvern Panalytical MagiX PRO, which is a wavelength-dispersive system. The loss on ignition (LOI) of the samples was measured after 30 min at 930 ^{o}C in air and then a major element analysis by XRF was done after borate fusion.

X-ray diffraction (XRD)

X-ray diffraction (XRD) measurements were performed to obtain information concerning the phase composition and the crystallite size distribution. Prior to the analysis, samples were loaded into the holder. The tube voltage and current of the instrument were set at 40 kV and 30 mA, respectively. The XRD instrument, which operated on a rhodium tube, had a K-beta filter mounted on it. The samples were run in a Rigaku XRD instrument equipped with a scintillation counter detector. The powder samples were scanned in the 0^o–75^o 2θ range at the rate of 0.2^o/min.

Brunauer-Emmet-Teller (BET)

The BET analysis measures the specific surface area and the pore volume of the iron catalyst. Prior to the analysis, the sample was de-gassed under vacuum at 190 ^{0}C for 8 h, to drive away any moisture in the samples. The surface area and porosity of the sample were measured with a TriStar II Micromeritics - Surface Area and Porosity analyser.

High Resolution Transmission electron microscopy (HRTEM)

High resolution transmission electron microscopy (HRTEM) was used to study the imaging structure of the iron catalyst. Samples were prepared by coating one drop of specimen solution onto a holey carbon coated nickel grid. This was then dried under a Xenon lamp for

about 10 minutes, where after the sample coated grids were analyzed under the microscope. Transmission electron micrographs were collected using an FEI Tecnai G2 20 field-emission gun (FEG) TEM, operated in bright field mode at an accelerating voltage of 200 kV. Energy dispersive x-ray spectra were collected using an EDS liquid nitrogen cooled Lithium doped Silicon detector.

3.3 Experimental setup

The synthesis gas (H_2/CO/ N_2 = 60%/30%/10%) and reducing gases were fed to the reactor using the Brooks mass flow controllers (Brooks Instrument 5850) for FT reaction and catalyst reduction respectively. A non-return valve was mounted after the mass flow control (MFC) channel to prevent the products from flowing back to the MFC (see **figure 3.1** below). Besides feeding the system with syngas, other channels were available to supply nitrogen to the reactor. Back pressure regulators were manually controlled to keep the reactor pressure at desired set point. All the experiments were conducted in a laboratory scale fixed bed reactor set-up, as shown in **Figure 3.1**.

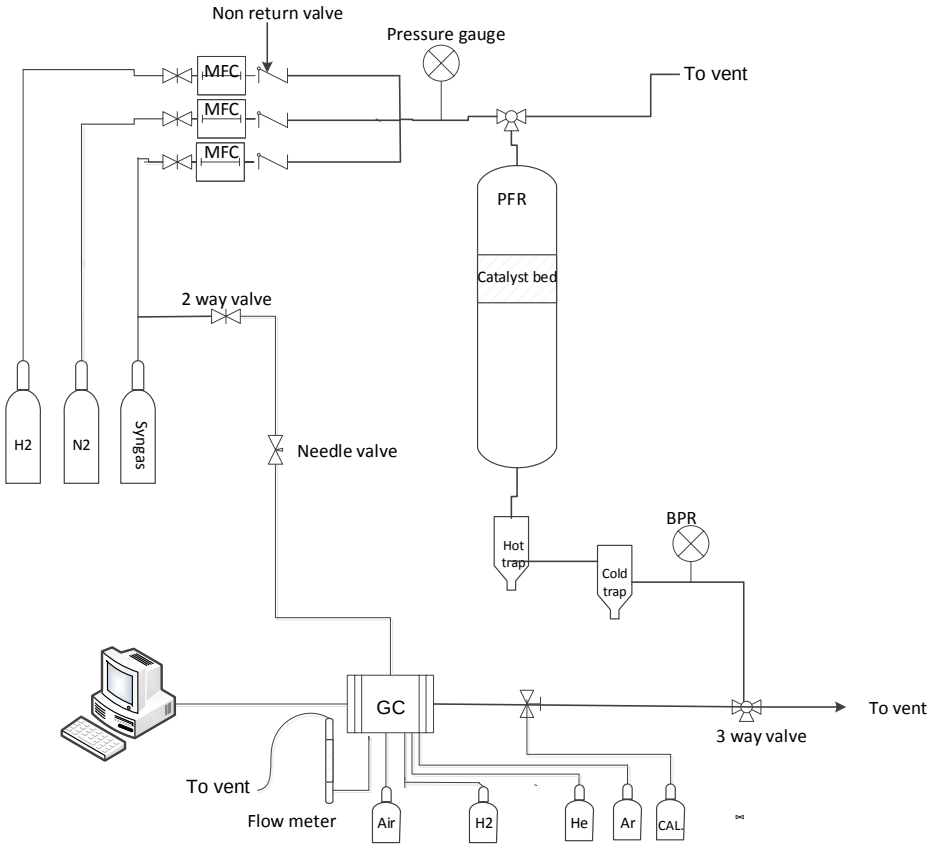
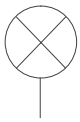


Figure 3.1: Flow scheme of the laboratory scale Fischer Tropsch rig with fixed bed reactor.



Fixed bed reactor



Back pressure regulator



Knock out pots



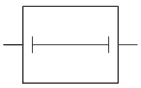
Three way valve



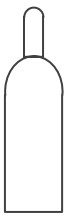
Non return valve



Two way valve



Mass flow controller



Gas Cylinder

3.3.1 FTS reactors

The reactor system and specification have been detailed in previous reports [4,8]. A brief description is provided below. A fixed bed reactor was used in this study. **Figure 3.2** shows the disassembled reactor with screwed end fittings. The reactor is made of a stainless-steel tube with heating coil (B) with a tube length of 204 mm and internal diameter of 8 mm, and screwed end fittings (A and C).

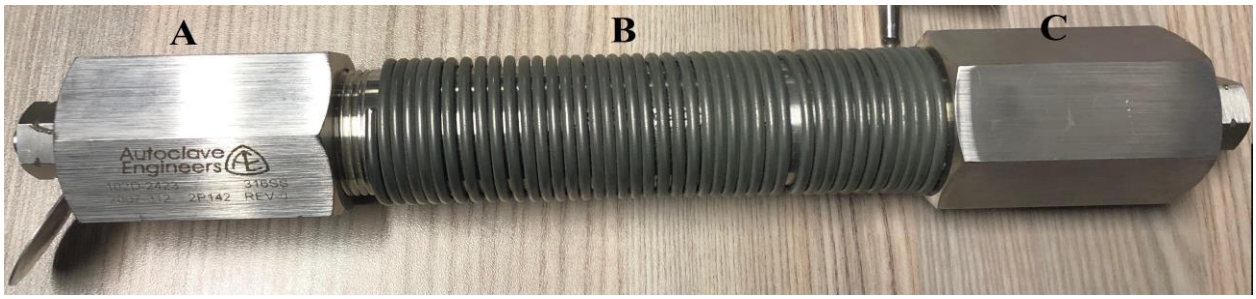


Figure 3.2: Schematic representation of the fixed bed reactor used in this study [6].

3.3.2 Catalyst loading into the disassembled reactor

The FT rig was tested with nitrogen gas to ensure that the system did not leak prior to the catalyst loading. Once all the fitting joints and lines were tight, the reactor was detached from the rig. The reactor was then disassembled in order to load the catalyst. **Figure 3.3** depicts a schematic representation of a loaded FT reactor with steel balls, iron catalyst and a thin layer of quartz wool. Measurements were done to locate the middle part of the reactor, then stainless steel balls were added to the middle of the reactor, and the thin layer of quartz wool was then pushed down the reactor shaft 6.35 mm (¼ inch). Thereafter, one gram of catalyst was loaded followed by another thin layer of quartz wool. Additional stainless-steel balls were inserted in the reactor tube to occupy the remaining volume, and then a final layer of quartz wool.

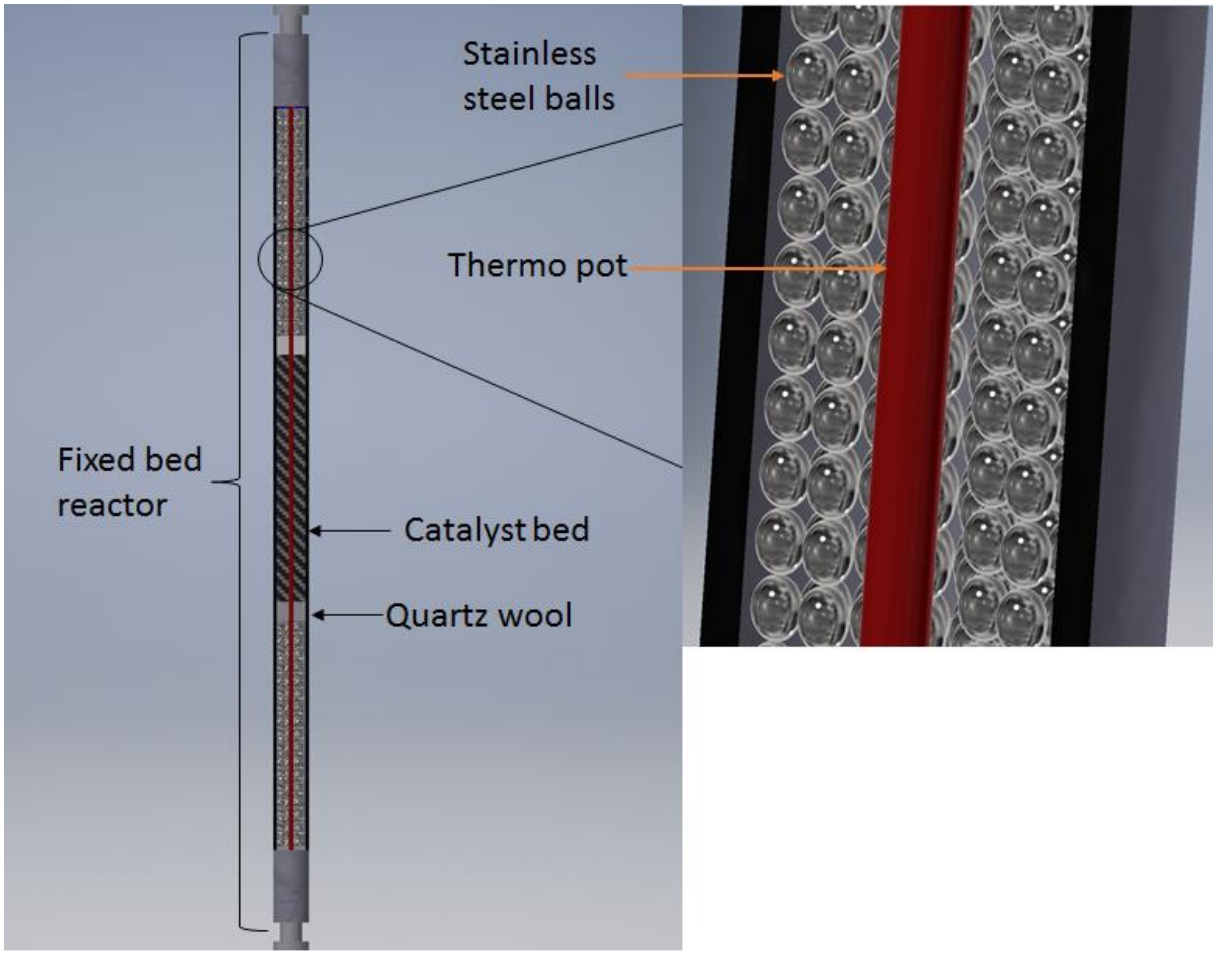


Figure 3.3: Representation of the FT reactor loaded with catalyst

Steel balls were used to keep the catalyst bed in position (in the middle of the reactor) and enhancing the gas distribution and flow patterns inside the reactor; the steel balls also preheated the syngas to the required experimental temperature, and they occupied all the tube length not taken up by the catalyst. This also contributed to maintaining isothermal conditions along the entire length of the reactors. Quartz wool was positioned at the catalyst–balls interfaces above and below the catalyst bed to prevent the catalyst from being blown out of the reactor tube. The temperature along the reactor tube was measured by a moveable thermocouple (K type of 1/16" OD thermocouple which was placed centrally in an axial position within the thermopot (1/8" OD thermopot). The temperature profile along the reactor before and during reaction was then measured. The difference between the central and wall control temperatures along the catalyst loaded part of the reactor was only 0.3 ^{o}C (the catalyst bed took less than 15 mm in the middle part of the reactor) so that the reactor could be regarded as isothermal. After loading the catalyst, the reactor was mounted back to the FT rig.

Then, leakage testing was conducted again for the reactor to make sure there was no leakage for the entire reactor system. The reactor was then insulated with a thermal blanket to prevent heat loss. The middle part of each reactor was heated with heating coils which were placed around the reactor and the top and bottom parts, forming the heating sheath. Temperature controllers were used to enable the setting of desired temperatures. These three zones (top, middle and bottom of the reactor) were monitored by the same kind of temperature controllers.

3.4 Fischer-Tropsch and catalyst evaluation

The experimental methodology carried out in this study was adopted from previously reported research by Gorimbo (2016)[4]. Various steps involved in the research are described in the next sections of the dissertation.

3.4.1 Catalyst reduction procedure

One gram of the Fe-Clino catalyst was loaded into the reactor. The catalyst was dried under the flow of nitrogen at a Gas Hourly Space Velocity (GHSV) of 2592 h^{-1}, 120 ^{o}C, for 2 hours at atmospheric pressure to get rid of the moisture which might have accumulated during catalyst loading. The catalyst was then reduced following similar conditions as for the drying process but the temperature of the reactor was increased from 120 ^{o}C to 440 ^{o}C at a heating rate of 10 ^{o}C/min. Following the H_2-TPR characterization results obtained, the reduction temperature for iron-based catalysts was set at 440 ^{o}C. We used UHP H_2 (AFROX (African Oxygen) Ltd., 99.999%) to reduce the catalysts with a constant GHSV of 2592 h^{-1}, keeping the temperature constant at 440 ^{o}C for 24 hours after which the reactor was cooled to below 100^{o}C. Then syngas was subsequently fed to the system during the Fischer-Tropsch reaction for the rest of the experiment.

3.4.2 FT synthesis

Fischer-Tropsch reaction started after the reduction when the pressure of the reactor was increased from atmospheric to 20.85 bar(abs) while the feed (syngas) continued to flow in the system. The FTS experiments were carried out under the reaction conditions listed in **Table 3.2** for **450** hours of time on stream (TOS). The results obtained from these FTS runs are

presented and discussed in Chapter 4. The syngas feed composition was 60% H_2, 30% CO and 10% N_2, and this corresponded to partial pressure of P_{H2} = 1.2, P_{CO} = 0.6 and P_{N2} = 0.2 bar within the reactor.

Table 3.2: Reaction conditions for the FT synthesis using Fe-Clino catalyst for 450 hours TOS

	Reaction condition
Reducing gas	Hydrogen
Reaction gas	Syngas (2:1)
Catalyst weight (g)	1
Temperature (°C)	250
GHSV (h^{-1})	2592 h^{-1}
Pressure (bar absolute)	20.85

3.4.2.1 Product separation and analysis

Several products in different phases are available inside the FT reactor. At the exit, two knockout pots were used to separate and collect the products. Hot trap was maintained at 150 ^oC in order to collect wax products whereas the cold knockout pot collected the liquid product at room temperature. Gaseous products were directed to the online gas chromatography (GC) instrument through the tail gas line heated at 150 ^oC to avoid any potential condensation and blockage of the tube. The tail gas was then analyzed and or vented.

The product analysis was carried out with a flame ionization detector (FID) and two thermal conductivity detectors (TCDs). One (TCD-A) of the TCDs used for online GCs, analysed CH_4, CO_2, N_2 and CO with UHP He as a carrier gas, while TCD-B was used to analyse H_2 with UHP Ar as a carrier gas using Teknokroma molecular sieve columns. Varian capillary columns were used in this FID system for the analysis of gaseous olefin and paraffin products (C_1–C_5). Samples from the tail gas were taken every 83 minutes via valves from the sampling loop. The excess gas from the sampling loop passed through a bubble flow meter to the vent. The products from the reactor were sampled periodically. Products from the two knockout pots (hot and cold) were collected and sent to the offline GC for analysis. A summary of the online GC settings and columns details is displayed in Table 3.3.

Table 3.3: Summary of the online GC settings and columns used

On-line GC	**DANI GC 1000**
Oven temperature programme	50 °C - 8 °C /min - 200 °C
Detector 1	FID, T - 220 ^oC
Column 1	Varian capillary column (Cp-Poraplot Q-HT), 12.5m*0.53mm* 20μm
Sample valve temperature	150 °C
Carrier gas	UHP Ar with flow rate of 30 mL (NTP)/min
Product analysis	C_1- C_5
Detector 2	TCD - A, T = 220 °C
Column 2	Teknokroma, porapack Q (Tmax: 250 °C), 80/100 mesh, 2m*1/8"*2.1mm
Column 3	Teknokroma, molecular sieve 13X (Tmax: 400 °C), 80/100 mesh, 2m*1/8"
Sample valve temperature	150 °C

Carrier gas	UHP Ar with flow rate of 30 mL(NTP)/min
Oven temperature programme	Hold at 50 °C for 8 min, heat to 200 °C at 8 °C /min, hold at 200 °C for 45 min
Product analysis	CH_4, CO_2, N_2, CO
Detector 3	TCD_B, T=220 °C
Column 4	Teknokroma, molecular sieve 5A (Tmax: 400 °C), 80/100 mesh, 1.5m*1/8"
Sample valve temperature	150 °C
Flame gas	Air with flow rate of 20 mL(NTP)/min and UHP H_2 with flow rate of 200 mL (NTP)/min
Carrier gas	UHP He, 30 mL (NTP)/min
Oven temperature programme	Hold at 50 °C for 8 min, heat to 200 °C at 8 °C /min, hold at 200 °C for 45 min
Product analysis	H_2

The chromatograms were recorded and used for the calculation of results. Typically, to properly quantify the product amounts, calibration was done using a special premixed gas with known molar fractions. The percentage composition of the calibration cylinder is given in Table 3.1. The amounts of the products were given by the integration of the peaks of known amount of analyte in standard chromatograms and those for the unknown samples from their chromatograms. The molar quantities of C_1 and C_2 hydrocarbons were determined directly and the remaining hydrocarbons (C_{3+}) in the gas phase were calculated using the calibration for C_2 and the corresponding FID response factors (Table 3.4).

It is important to note that the focus of the current dissertation was on light hydrocarbons monitored by the online GC only. Although the liquid and solid (wax) hydrocarbons were obtained but are not part of the results presented and discussed in this study. Furthermore, the

hydrogen conversion is not reported due to analysis limitations. Typical chromatograms from the TCDs and FID are given in **Figures 3.4** to **3.6**, respectively.

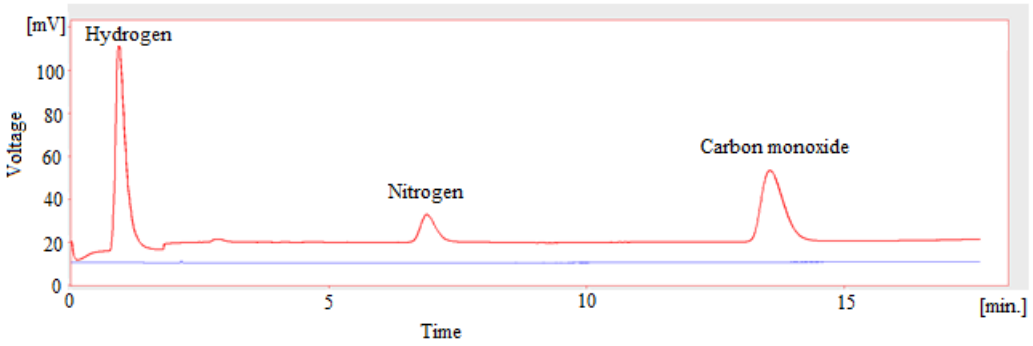


Figure 3.4: Typical online analysis of the syngas (red line from TCD detector and blue line from that of FID)

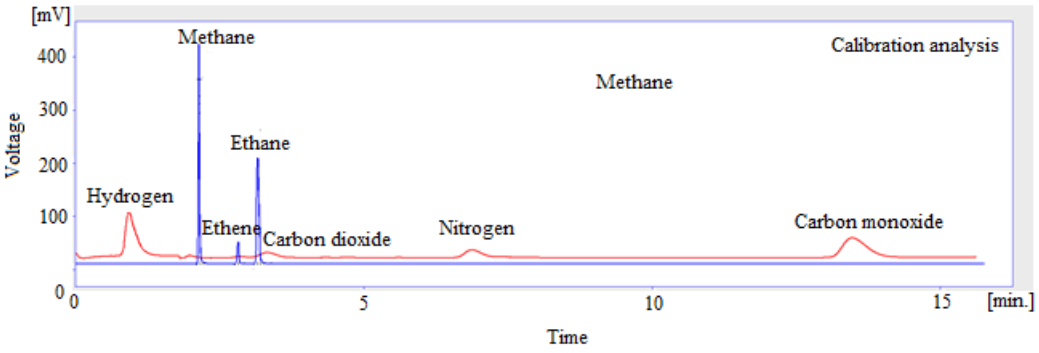


Figure 3.5: Typical online analysis of the calibration gas (red line from TCD detector and blue line from FID)

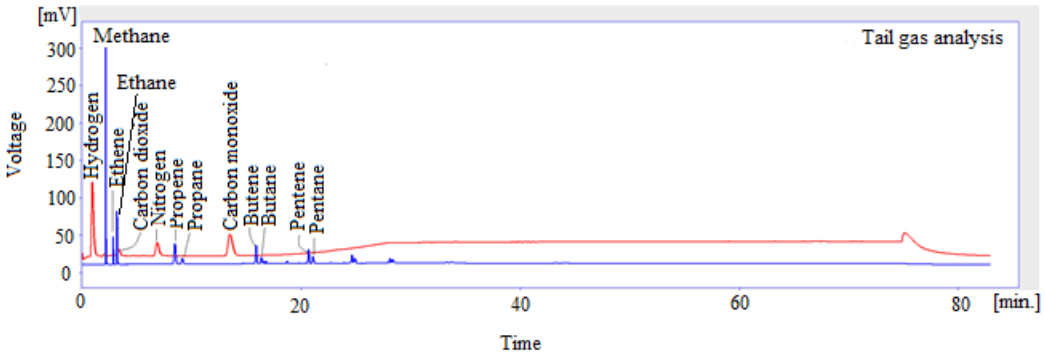


Figure 3.6: Typical online analysis of the tail gas (red line from TCD detector and blue line from FID)

3.4.2.2 Product storage

The solid and liquid products were collected in glass vials sealed with paraffin paper, labelled with stickers and stored in a refrigerator awaiting analysis

3.4.2.3 Calculation

The data collected from the on-line GC were quantitatively processed. Nitrogen (N_2 10 vol %) contained in syngas feed of FT experiments was used as the internal standard for the measurements of TCD data. The molar flow rates of the various reactants and products were determined and these enabled the calculations of other factors such reactants conversions and rates of consumption, rates of the products and selectivity to the products, and mass balance. Mass balance calculations including the conversion of reactants CO were determined using the equations 3.3 to 3.8. These calculation are similar to those used by the previous researchers[3,8–10]

CO conversions, %CO, was calculated as follows:

$$\%\ CO = \frac{F_{in} X_{co,in} - F_{out} X_{co,out}}{F_{in} X_{co,in}}$$ Equation 3.3

where: F_{in} and F_{out} means flowrate in and out respectively

$X_{co,in}$ is the molar fraction of CO in the reactor inlet gas feed;

and $X_{co,out}$ is the molar fraction of CO in the reactor outlet gas stream.

The CO consumption rate is calculated as follows:

$$r_{co} = \frac{F_{out} X_{co,out} - F_{in} X_{co,in}}{m_{cat}}$$ Equation 3.4

where:

r_{co} is the rate of CO consumption, mol/(min.gcat)

m_{cat} is the mass of the catalyst used in this reaction, in gram.

The formation rate of gas a product θ_i, mol/(min.gcat) is given by:

$$r_{\theta_i} = \frac{F_{out} X_{\theta_{i,out}}}{m_{cat}}$$ Equation 3.5

where:

$X_{\theta_{i,out}}$ is the molar fraction of θ_i in the reactor outlet gas stream.

The product selectivity was calculated on the moles of carbon basis, as follows:

$$Sel\ (\theta) = \frac{[nC]_\theta}{-r_{co} \times t \times m_{cat}}$$ Equation 3.6

where:

$Sel\ (\theta)$ represents the selectivity of product θ and $[nC]_\theta$ represents the moles of carbon contained in the product θ.

C_1–C_5 products quantified on the FID detector, from which it was possible to determine the C_{5+} selectivity (S_{C5+}). The CO_2-free S_{C5+} (i.e., S_{C5+} if excluding CO_2 from the C-atom balance) is defined as follows[4]:

$$S_{C_{5+}} = 100 - \left(S_{C_1} + S_{C_2} + S_{C_3} + S_{C_4}\right)_{CO_2 free}$$ Equation 3.7

The response factors as reported by [11] were used to correct hydrocarbons based on the known areas of C_2H_4 (olefin) and C_2H_6 (paraffin) in the calibration.

Table 3.4: Response factors for hydrocarbon products

Carbon number	Olefin	Paraffin
2	1	1
3	0.7	0.74
4	0.55	0.55
5	0.47	0.47
6	0.4	0.4
7	0.35	0.35
8	0.32	0.32
9	0.28	0.28
10	0.24	0.24
11	0.21	0.21
12	0.19	0.19
13	0.18	0.18
14	0.17	0.17
15	0.15	0.15

Olefin/paraffin ratio

Olefin/paraffin (O/P) ratio was calculated as follows, considering the relative molar amount for the same carbon number in the outlet stream:

$$\frac{O_n}{P_n} = \frac{N_{C_nH_{2n}}}{N_{C_nH_{2n+2}}}$$ Equation 3.7

Olefin/olefin ratio

Olefin/olefin (On/On-1) ratio looked at the relative molar amount for the immediate neighbouring olefins in the outlet stream, which was calculated as follows:

$$\frac{O_n}{O_{n-1}} = \frac{N_{C_nH_{2n}}}{N_{C_{n-1}H_{2(n-1)}}}$$ Equation 3.8

References

[1] H. Li, B. Hou, J. Wang, C. Qin, M. Zhong, X. Huang, L. Jia, D. Li, Mol. Catal. 459 (2018) 106–112.

[2] K. Keyvanloo, B. Huang, T. Okeson, H. Hamdeh, W. Hecker, Catalysts 8 (2018) 77.

[3] A.A. Muleja, Study of the Selectivity To Light Hydrocarbons in Fischer-Tropsch Synthesis, University of the Witwatersrand, 2016.

[4] J. Gorimbo, thesis (2016) 26–215.

[5] J. Gorimbo, X. Lu, X. Liu, D. Hildebrandt, D. Glasser, Appl. Catal. A Gen. 534 (2017) 1–11.

[6] J.W. Niemantsverdriet, A.M. Van Der Kraan, W.L. Van Dijk, H.S. Van Der Baan, J. Phys. Chem. 84 (1980) 3363–3370.

[7] J.P. Reymond, P. Mériaudeau, S.J. Teichner, J. Catal. 75 (1982) 39–48.

[8] Y. Yao, Fischer-Tropsch Synthesis Using Co 2 -Containing Syngas Mixtures Over Cobalt and Iron Based Catalysts, 2011.

[9] J. Gorimbo, A. Muleja, X. Liu, D. Hildebrandt, Int. J. Ind. Chem. (2018).

[10] X. Lu, Fischer-Tropsch Synthesis: Towards Understanding., 2012.

[11] W.A. Dietz, J. Chromatogr. Sci. 5 (1967) 68–71.

CHAPTER 4

RESULTS AND DISCUSSION

4.1 Characterization of fresh prepared catalysts

4.1.1 Temperature programmed reduction

The temperature programmed reduction (TPR) was used to measure the maximum reduction temperature of the prepared catalyst in this study. The resulting TPR profile is depicted in Figure 4.1. The two-stage reduction of prepared catalyst was observed corresponding to the following representation: $Fe_2O_3 \rightarrow Fe_3O_4 \rightarrow Fe$. This two-stage reduction agrees with what has been postulated in the literature at reduction temperatures less than 570 °C, with a three-stage reduction mechanism ($3Fe_2O_3 \rightarrow 2Fe_3O_4 \rightarrow 6FeO \rightarrow 6Fe$) observed at temperatures higher than 570 °C[1–4].

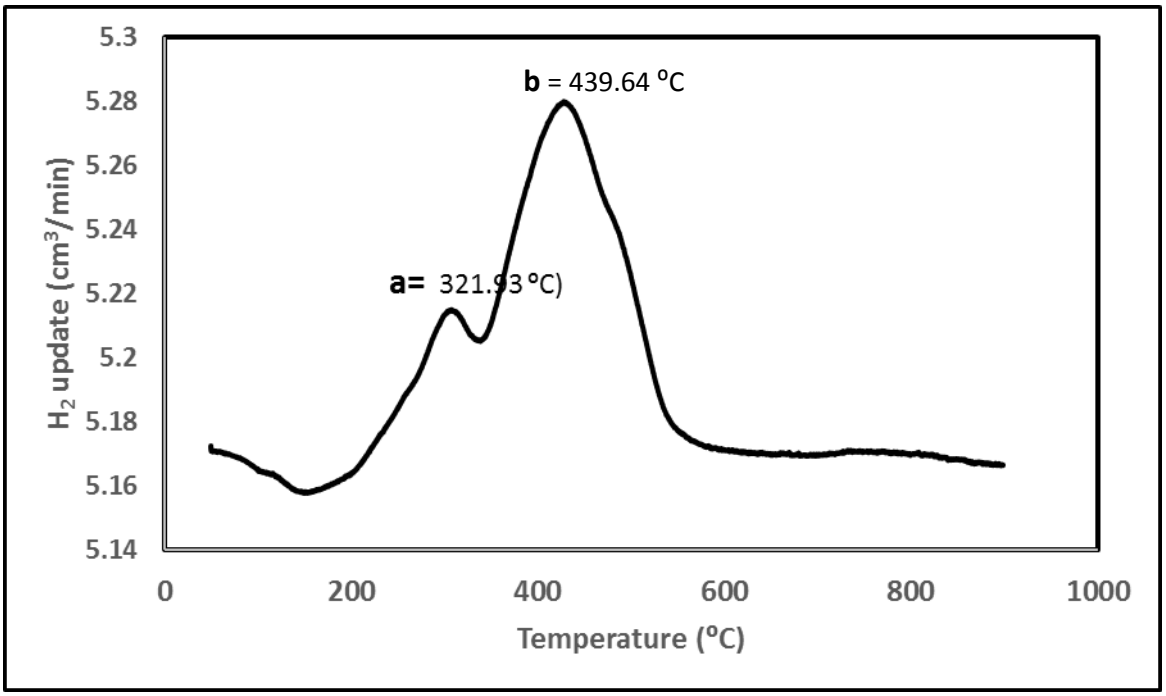


Figure 4.1: H_2 -TPR profiles of the calcined Iron catalysts

As per Figure 4.1, the peaks are attributed to the following reactions:

Peak a: $3Fe_2O_3 + H_2(g) = 2Fe_3O_4 + H_2O(g)$ $\Delta G_{321.93°C} = -56.022$ kJ equation 4.1

Peak b: $Fe_3O_4 + 4H_2(g) = 3Fe + 4H_2O(g)$ $\Delta G_{439.64°C} = 43.206$ kJ equation 4.2

The conversion of hematite (Fe_2O_3) to magnetite (Fe_3O_4) is spontaneous as shown by the negative delta ΔG value in Equation 4.1, this peak formation (near 321.93°C) is formed regardless of the external factors such as H_2/ H_2O ratio[5].

The second peak formation attributed to the reduction of magnetite (Fe_3O_4) to metallic iron (Fe) at temperatures 439.64 ^{0}C is more sensitive to the H_2/ H_2O as indicated by the positive ΔG values. The formation of metallic Fe from magnetite thermodynamically disfavoured. These calculated ΔG values imply that reduction process should yield only a single peak (hematite to magnetite). To explain the existence of the second peak (peak due to reduction of magnetite to metallic Fe) and to corroborate the literature on insitu reduction studies, Gorimbo (2018)[5] justified the formation of metallic iron using stability diagrams taking into account the H_2/H_2O partial pressures during reduction. For each mole of hydrogen consumed a mole of H_2O is produced, so the formation of metallic Fe could be a function of the H_2/ H_2O ratio.

Reduction peak temperature indicates the ease of reduction and degree of interaction between different species present in the catalyst sample. A higher reduction temperature indicates higher difficulty in reduction which can be attributed to the greater degree of interaction between the iron and the Clinoptilolite.

The reduction temperature was high (440 ^{o}C) probably because copper was not added. It is also important to note that in an attempt to reducing reduction temperature by adding copper[6][7] metallic iron which is formed will sinter easily if the reducing temperature is too high. However, this sintering phenomenon is not as critical when activating with carbon monoxide or syngas as in this study because iron carbides are formed and they are not as susceptible to sintering[6]. For this kind of support used in this study sintering is therefore a function of SiO_2/ Al_2O_3 ratios, with lower ratios being idea due to the strong metal-support interaction in Al_2O_3 than SiO_2[8].

4.1.2 X-ray fluorescence characterization of natural zeolite

X-ray fluorescence (XRF) measurement of the samples was carried out to identify typical oxides present in the natural and treated clinoptilolite. Table 4.1 shows a chemical composition of the catalyst and support obtained with XRF.

The analysis (Table 4.1) of Clino-support and Fe-Clino catalyst precursor shows that the Fe_2O_3 added by impregnation method as explained in Chapter 3 is greatly in excess (more than 10% added) even if the contribution from the support is taken into account. The catalyst precursor analysis yielded a loading of 13.08 mass.%, hence the excess of 3.08 mass% is attributed to analytical error or due to contamination during sample preparation.

Table 4.1: Chemical Composition (mass. %) of treated Clinoptilolite sample

Composition	**SiO_2**	**Al_2O_3**	**Fe_2O_3**	**MnO**	**MgO**	**CaO**	**Na_2O**	**K_2O**	**TiO_2**	**LOI**
Mass. (%)										
Fe/Clino	61.90	10.39	14.27	0.03	*0.66*	1.00	1.53	3.33	0.12	6.15
Fresh Clino	71.34	12.17	1.19	0.02	*0.77*	1.18	1.75	3.78	0.13	7.31

In this study, The XRF analysis is very important because the researcher can deduce the molecular ratio SiO_2/ Al_2O_3 of the zeolite. This value can be highly significant to describing the physisorption or chemisorption interaction of the metal loaded with the zeolite. From the XRF analysis conducted on the natural zeolite, the elements present in the natural zeolite are identified. Moreover, it is noteworthy that the chemical analysis obtained by the XRF technique are qualitatively and quantitatively significant. The molecular ratio SiO_2/ Al_2O_3 of Fe-Clino is then determined to be about 5.96 and that of the Clino-support is 5.86. It is of importance in Fischer Tropsch catalyst to have a high SiO_2/ Al_2O_3 ratio as significant support interactions on the reduction of iron oxide species occur

at low ratio. Metal oxide interaction were observed in this order Al_2O_3 > TiO_2 > SiO_2. These interactions often make the catalyst difficult to reduce[9].

XRF analysis showed that metal oxides that are used as promoters are within the correct FT range (<5%) as displayed in Table 4.1[10]. Therefore, there is a need to investigate the effect of this natural zeolite in FTS. Effective reduction of the active phase plays an important role in optimizing catalyst performance, while the addition of small quantities of promoters during the formulation of the catalyst have been found to significantly enhance the reducibility of Fe catalyst. The Clinoptilolite samples from Pratley Kwazulu Natal gave a molecular ratio $SiO_2/A1_2O_3$ of 5.77[11] close to the sample used in this study which were obtained from Krugersdorp, Johannesburg mine. Fe-Clino consists principally of most of the supports used in catalyst making, silica being the most common one. In addition, small amounts of promoters, Na_2O, K_2O, MgO and MnO are also present. These inert contaminants, making up less than 5% by mass could play significant role in the catalytic properties of the FT catalyst.

4.1.3 **X-ray Diffraction**

The X-ray diffraction (XRD) patterns of the natural clinoptilolite zeolite used as catalyst support and the Fe- Clino catalyst were found to be similar as illustrated in Figure 4.2. except that the relative intensities of the peaks due to magnetite increased. The fact that the XRD patterns of the clinoptilolite samples remained unchanged after impregnation with iron except for the intensity change, indicates that their crystalline structure remained intact after the impregnation. The lowering of peak intensities occurred in the Fe-Clino at 2-theta 11.35^0, 22.59^0 and 28.30^0 (see Figure 4.2). XRD showed that the clinoptilolite has been found to be ordered in the monoclinic space group C2/m whereas after Fe impregnation (Fe-Clino) it adopted an orthorhombic space group Imma for packing determination.

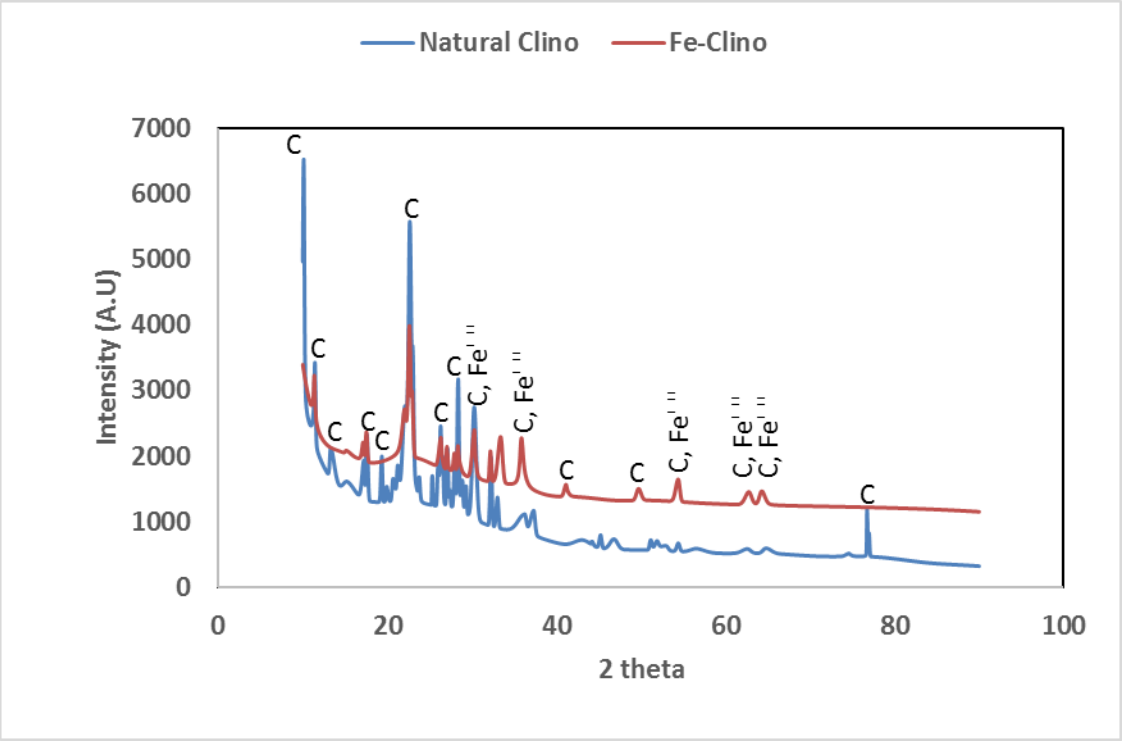
Another important measure which affects the catalytic activity and selectivity is the crystallite sizes which was calculated to be in the range of 11.36 - 14.62 nm (obtained from XRD). This value is not far from what is regarded as idea size in the literature[12]. The

particle sizes are calculated using Scherrer's equation [13,14] by taking into account the most intense peak.

$$\tau = \frac{K\lambda}{\beta \cos\theta}$$

Equation 4.3

Where τ τ is the mean size of the ordered (crystalline) domains, which may be smaller or equal to the grain size; K is a dimensionless shape factor, with a value close to unity. The shape factor has a typical value of about 0.9, but varies with the actual shape of the crystallite; λ is the X-ray wavelength; β is the line broadening at half the maximum intensity (FWHM), after subtracting the instrumental line broadening, in radians. This quantity is also sometimes denoted as Δ(2 θ); θ is the Bragg angle.



C = Clinoptilolite-Na : $Fe^{1\,11}$ = Iron diiron(III) oxide, magnetite low

Figure 4.2: X-ray diffraction patterns of Natural Clinoptilolite and Fe- Clinoptilolite catalyst

4.1.4 High resolution Transmission Electron Microscopy (HRTEM)

HRTEM images of all the iron particles on the fresh show fairly negligible size difference even if the used one was subjected to FTS reaction. The average crystal size of the particles range 9.83 -11.649 nm and around 10.10 nm for used and fresh catalyst respectively (see **figure 4.3**). These measured sizes are almost of the same magnitude as that calculated from the XRD data.

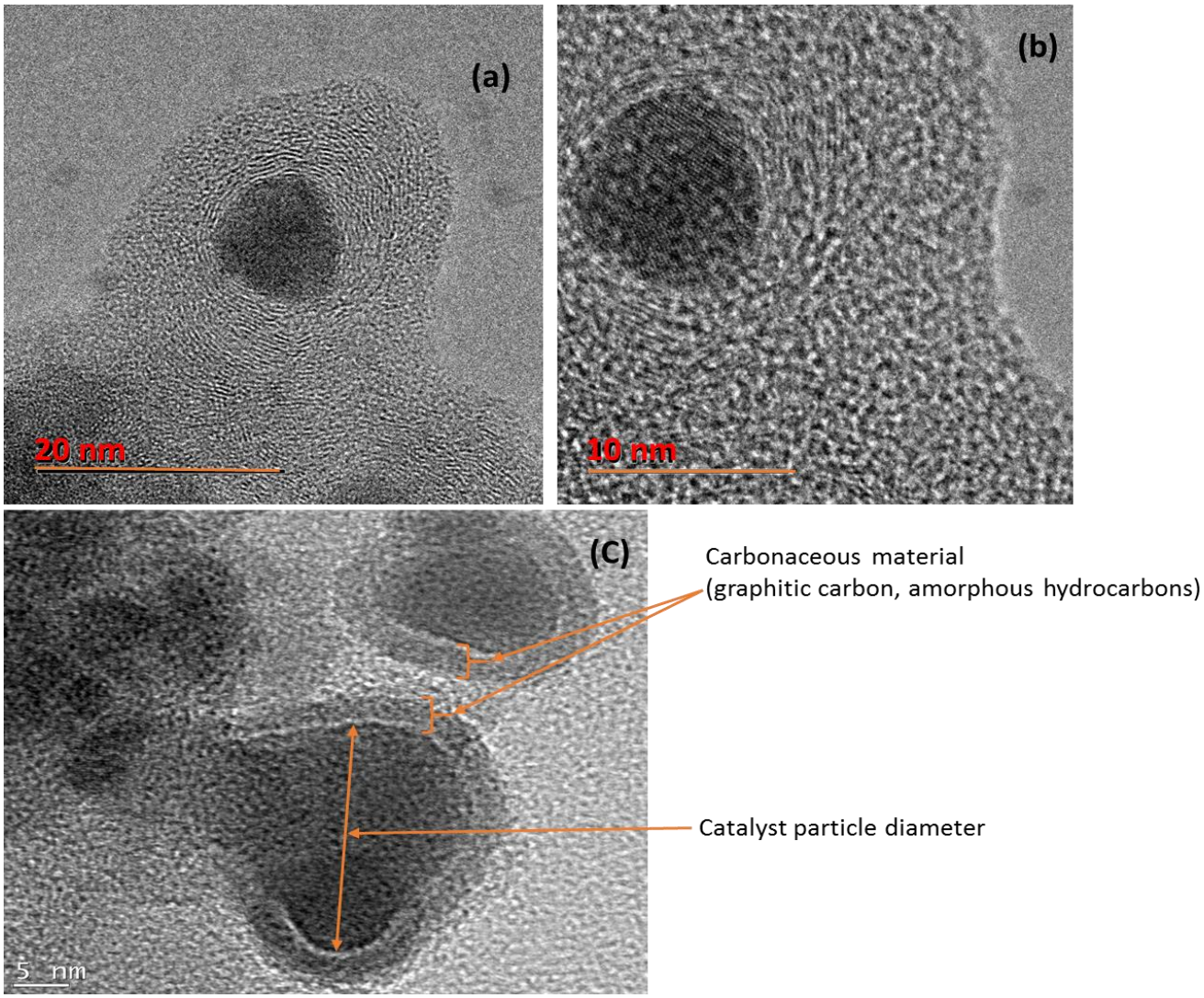


Figure 4.3: HRTEM images of the (a,b) fresh catalysts at 20 nm and 10 nm respectively and (c) used catalyst at 5 nm.

Amorphous deposits on the catalyst particles have been described extensively. It is generally accepted that such layers can be formed during FTS and some researchers refer

to it as the liquid layer [15][16]. The HRTEM images confirm these suggestions. Although long chain hydrocarbons are the desired products in FTS, those of very high molecular weight can accumulate on the surface blocking sites and/or block small mesopores retarding the rate of diffusion of the reactants from catalyst particles.

Images in figure 4.3 shows a carbonaceous material layer around catalyst particle of ca. 2.5 nm thickness. This FT hydrocarbon waxes which accumulate on the surface can potentially retard the rate of diffusion of the reactants in and out of the catalyst active sites and slow down the reaction[16] [17]. The hydrocarbons are not directly connected to the catalyst deactivation, they are just slowing down an already slow reaction[18], which seem to be negligible deactivation and it will be shown in the FT results. However, polymeric carbon formation could lead to deactivation since it is comparatively denser than amorphous carbon. It is therefore reasonable to expect that carbon is a possible cause of deactivation since carbon may interact with the metal under reaction conditions and form inactive species that may act as reaction inhibitors (e.g. amorphous, graphitic or other surface carbon species)[18].

4.1.5 **Brunauer-Emmett-Teller (BET)**

The Brunauer–Emmett–Teller (BET) method was used to calculate the surface area and single point method was employed to obtain the total pore volume. The pore structure of the clinoptilolite (Pratley Mining Company, Krugersdrop, South Africa) was characterized by N_2 physisorption and the results are presented in Table 4.2. The surface area obtained was 22.04 m^2/g, and its pore volume was 0.071 cm^3/g. The current clinoptilolite gave a comparatively high surface area than samples collected from KwaZulu-Natal which had 17.52m^2/g as previously reported. [19] However, the samples collected from Heidelberg-Riversdale Area in the Western Cape, South Africa had a high surface area of 33.4 m^2/g[20]. On the other hand, the Fe-Clino catalyst surface area is comparable to the catalyst used in studies by HaijunWan, (2008)[7].

Table 5.2: BET characteristics of the catalyst used

Surface Area	**Values**
Single point surface area at P/Po = 0.199:	22.04 m^2/g
BET Surface Area:	22.60 m^2/g
BJH Adsorption cumulative surface area of pores between 1.7 nm and 300.0 nm diameter:	17.04 m^2/g
BJH Desorption cumulative surface area of pores between 1.7 nm and 300.0 nm diameter:	23.55 m^2/g
Pore Volume	
Single point adsorption total pore volume of pores less than 176.0339 nm diameter at P/Po = 0.989:	0.071 cm^3/g
BJH Adsorption cumulative volume of pores between 1.7000 nm and 300.0000 nm diameter:	0.0778 cm^3/g
BJH Desorption cumulative volume of pores between 1.7 nm and 300.0 nm diameter:	0.084 cm^3/g
Pore Size	
Adsorption average pore width (4V/A by BET):	12.62 nm

BJH Adsorption average pore diameter (4V/A):	18.27 nm
BJH Desorption average pore diameter (4V/A):	14.24 nm

4.2 FT results

4.2.1 Catalytic activity

The catalyst activities measured by CO conversion, water gas shift (WGS) selectivity and FT selectivity as function of TOS during FTS is shown in Figure 4.4. Separatly, the water-gas shift (WGS) selectivity is the ratio of CO_2 production to total CO consumption and FT selectivity was determined as a function of CO converted to hydrocarbons. The three graphed parameters showed desirable distribution with the WGS selectivity less than 20% for conversions averaging 11.09±0.49%.

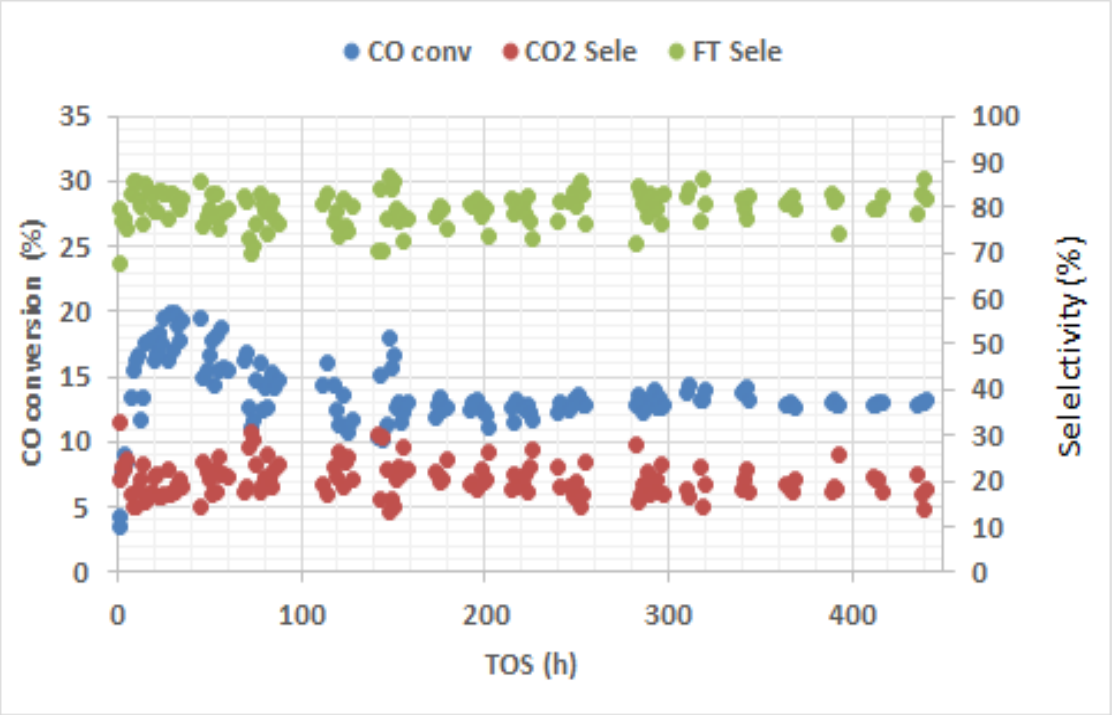


Figure 4.4: CO conversion, WGS selectivity and FT selectivity under operating conditions: 250 °C, 2592 h-1 at 20.85 bar (abs).

An increase in WGS selectivity can be used as a measure of catalyst deactivation by oxidation as magnetite is known to be the active catalyst for WGS reaction[21–23]. In this study, the deactivation of the catalyst was not observed. Instead the results tabulated in table 4.3 showed that the catalyst activity in particular the Fischer Tropsch selectivity was comparatively higher than water gas shift reactions for Fe-Clino catalyst.

Table 4.3: Averaged CO Conversion, WGS and FT selectivity with standard deviation errors obtained after 450 h TOS.

Parameter	Average±SD
CO conversion (%)	11.09±0.49
WGS Selectivity (%)	19.02±2.61
FT Selectivity (%)	80.98±2.61

4.2.2 **Rates**

The reactant (CO) consumption rate $i\ (r_{reactant(i)}, mol/min \cdot gcat$ was calculated as follows:

$$-r_{reactant\,(i)} = \frac{F_{in} X_{reactant\,(i),in} - F_{out} X_{reactant\,(i),out}}{m_{cat}} \qquad \text{Equation 4.3}$$

Where m_{cat} is the mass of the catalyst used in the reaction in grams.

To augment Figure 4.4 and Table 4.3 results Figure 4.5 shows the variation of FTS reaction rates and WGS reaction with time on stream. These variations have been calculated from experimentally observed quantities by the following identities:

$$r_{WGS} \equiv r_{CO_2}$$ Equation 4.4

And

$$r_{FTS} \equiv r_{CO} - r_{CO_2}$$ Equation 4.5

Where r_{CO_2} is the rate of CO_2 formation and r_{CO} is the rate of CO consumption.

The FTS reaction produces water, which is a necessary reactant for the WGS reaction to proceed, thus the rate and extent of the WGS reaction is limited by the amount of water formed by the FTS. Since water is not supplied to the reactor, the stoichiometry of the FTS and WGS reactions agrees with the following condition:

$$r_{WGS} \ll r_{FTS}$$ Equation 4.6

The production of the undesired CO_2 is as a result of the presence of magnetite fractions in the catalyst bed which catalyse the Boudouard reaction. The behaviour of Fe-Clino catalyst used in these experiments behaved differently from the other used iron catalyst based on different supports for instance, the 10% Fe loading on Silica reduced with H_2 reported in studies by Gorimbo et al, gave a conversion of ca. 54.47% [24].

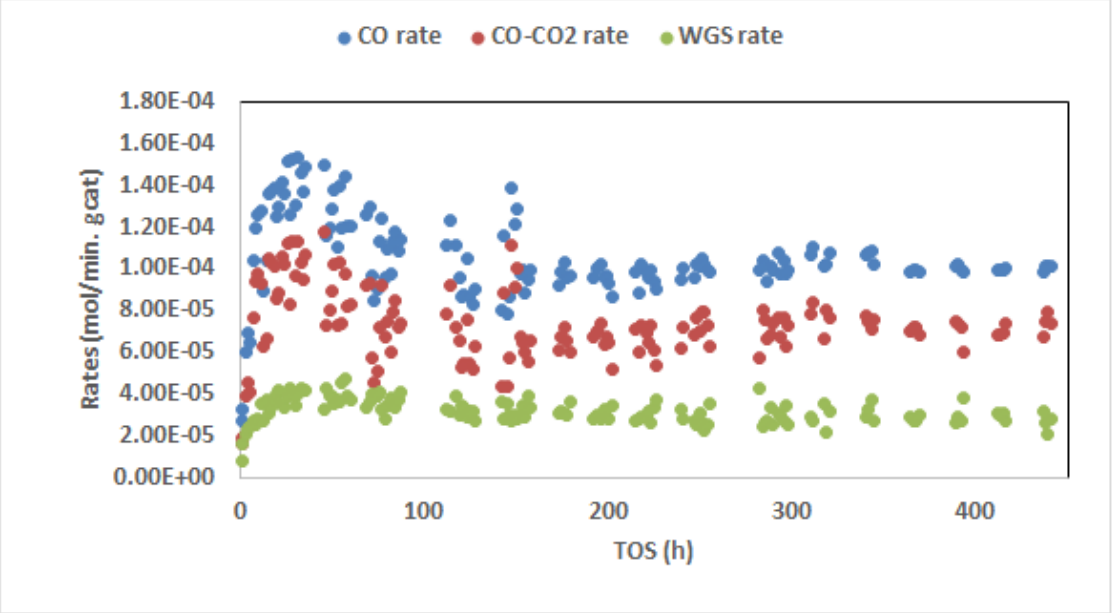


Figure 4.5: CO consumption rate, WGS rate and FTS rate under operating conditions: 250 °C, 2592 h-1 at 20.85 bar (abs).

Table 4.4: Averaged CO consumption rate, WGS rate and FT rate with standard deviation errors obtained after 450 h TOS.

Parameter	Average±SD
CO rate (mol/min.gcat)	$(1.02 \pm 0.037) \times 10^{-4}$
WGS rate (mol/min.gcat)	$(2.93 \pm 0.39) \times 10^{-5}$
FT rate (mol/min.gcat)	$(7.24 \pm 0.52) \times 10^{-5}$

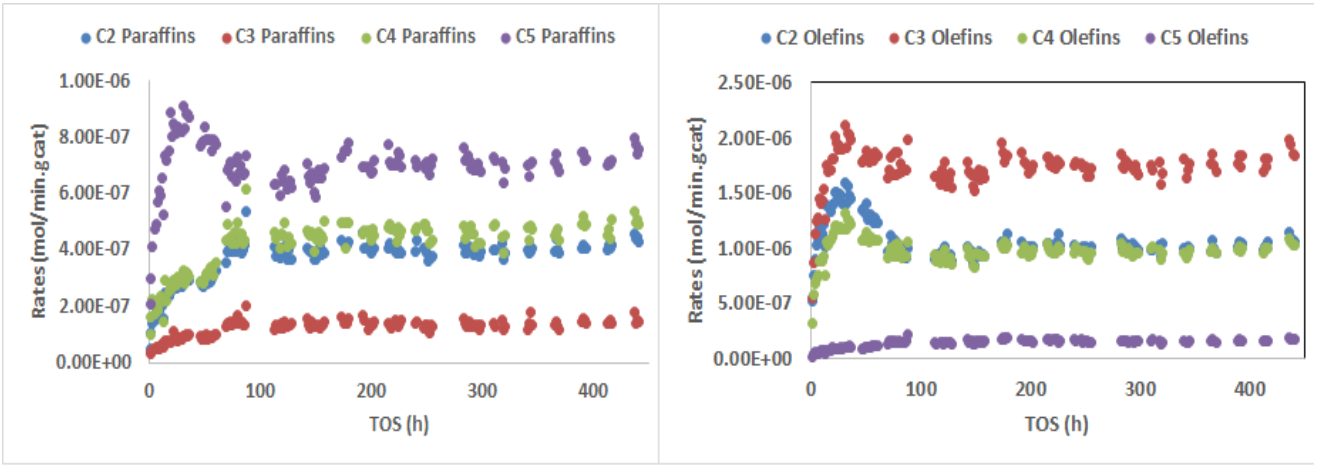


Figure 4.6: Paraffin production rate(left) and olefins production rate (right) for TOS of 450 h.

Table 4.5: Averaged paraffins and olefin production rate with standard deviation errors obtained after 450 h TOS

Species	**Production rate±SD (mol/min.gcat)**	
	Paraffins	**Olefins**
C2	$(3.93 \pm 0.77) \times 10^{-7}$	$(9.83 \pm 1.91) \times 10^{-7}$
C3	$(1.40 \pm 0.15) \times 10^{-7}$	$(1.76 \pm 0.09) \times 10^{-6}$
C4	$(4.67 \pm 0.35) \times 10^{-7}$	$(9.82 \pm 0.40) \times 10^{-7}$
C5	$(1.62 \pm 0.11) \times 10^{-7}$	$(7.14 \pm 0.33) \times 10^{-7}$

The trend that can be deduced from the values in Table 4.5 is as follows:

$C_3 < C_2 < C_4 < C_5$ paraffin trend

$C_5 < C_4 < C_2 < C_3$ Olefin trend

These trends clearly indicate the negating behavior in the production of paraffins and olefins. The production rates of paraffins tend to increase from C_2 to C_5 and an opposite trend is observed for olefins.

The products distribution of hydrocarbons formed are summarised in Table 4.6 for both the light hydrocarbons and the heavy hydrocarbons. The WGS selectivity is almost of the same magnitude as the selectivity to light hydrocarbons (CH_4 + C_2 – C_4). WGS reaction and methane contribute a quarter in terms of product selectivity meaning ca 25% of the CO used went to undesirable products for the duration of the run recorded.

Table 4.6 shows that the methane content was very low, while the hydrocarbon content in the C_2–C_4 range accounted for about 15 wt%. The α-olefins in this carbon number range are a high value-added industrial feedstock.

Table 5.2: Summary table of Fe-Clino catalyst activity and selectivity

Catalyst time on stream (h)	450
CO conversion (%)	11.09±0.49
Hydrocarbon selectivities (wt.%)	80.98±2.61
CO_2	19.02±2.61
CH_4	6.68±0.43
C_2–C_4	14.78±0.94
C_{5+}(excluding CO_2)	79.17±1.31: (60.15±3.09 including CO_2)

Reaction condition: 250 ^{0}C, 2592 h^{-1}, 20.85 bar (absolute), syngas (H_2:CO = 2 mol/mol)

4.2.3 **Ratios**

Olefin versus paraffin production was measured for hydrocarbons of four different lengths, C_2 to C_5. Independent of catalyst, the P/O-ratio was highest for hydrocarbons of C_4, and lowest for C_3 hydrocarbons. The following P/O ratio trend is observed $C_3 < C_5 < C_2 < C_4$.

Figure 4.7 and table 4.7 shows the P/O-ratios at steady-state for the Fe-Clino catalysts. From these it is evident that the preferred olefinic products were obtained under the operating conditions considered in this study.

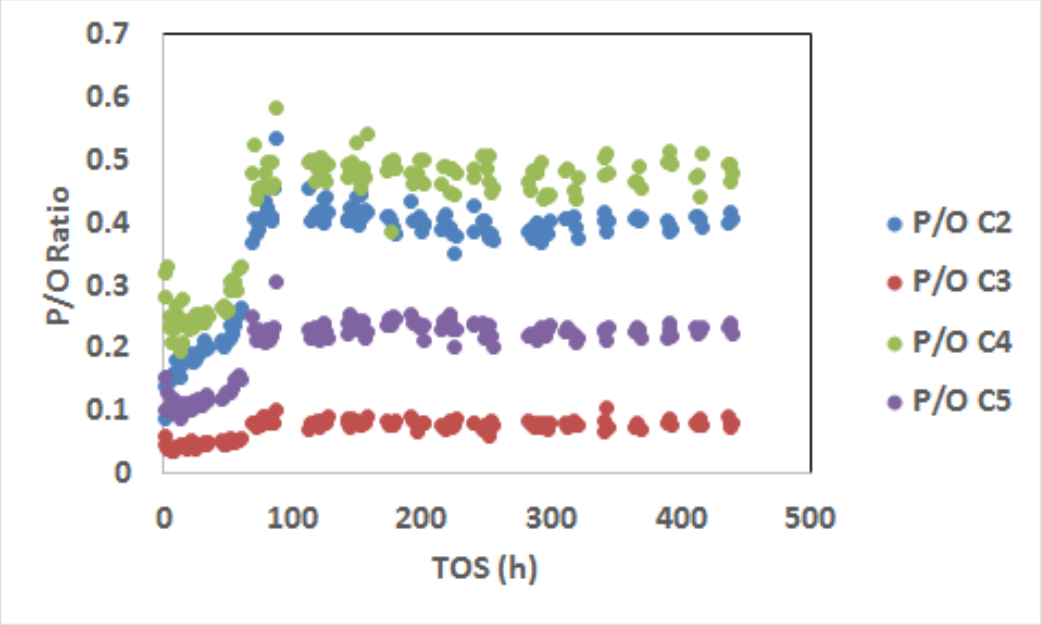


Figure 4.7: Paraffin/Olefin ratios under the following FT reaction condition: 250 ^{0}C, 2592 h-1, 20.85 bar (absolute), syngas (H2:CO = 2 mol/mol)

Figure 4.7 shows the molar paraffin to olefin (P/O) ratio as a function of time on stream over an Iron based catalyst. The results suggest that the paraffin to olefin ratio does not significantly change as a function of time on stream.

Table 4.7: Averaged P/O ratio for C2 to C5 with standard deviation error.

Parameter (P/O)	Average±SD
C_2	0.40±0.01
C_3	0.08±0.01
C_4	0.48±0.02
C_5	0.23±0.01

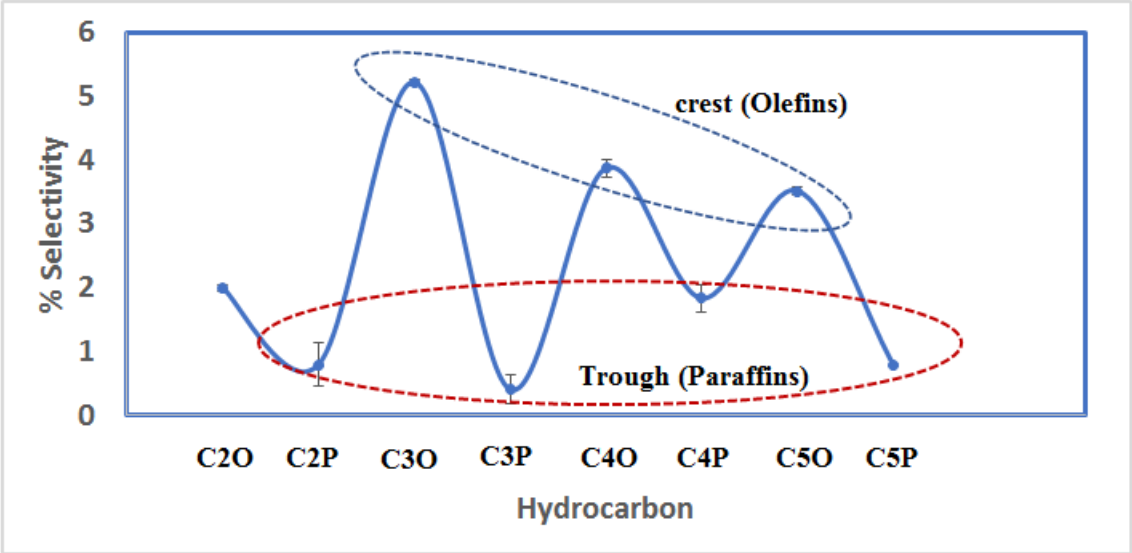


Figure 4.8: Wave like behavior of light hydrocarbon selectivity distribution

Linear α-olefins are highly valuable chemicals and intermediates for the production of many industrial and consumer products[24,25]. Even numbered carbon α-olefins (C_4, C_6, and C_8) are used as co-monomers for ethylene and propylene polymerization[25]. The typical product distribution of light hydrocarbons illustrated in Figure 4.8 indicate that for

each carbon number from C_2 to C_5 the selectivity for α-olefin was always more than that for n-paraffin.

Typical product distribution in **Figure 4.9** shows a typical GC chromatogram of the gaseous products from gas-FTS. In the whole carbon number range, the α-olefin, n-paraffin peaks and isomers appeared in multiples and the peak areas of the olefins being the largest. This result was obviously different from the other GC spectrum for the products of traditional FTS due to a number of isomers found using Fe-Clino catalyst [27][15]. An apparent commonality is the peak area of the α-olefin which decreased with increasing carbon number.

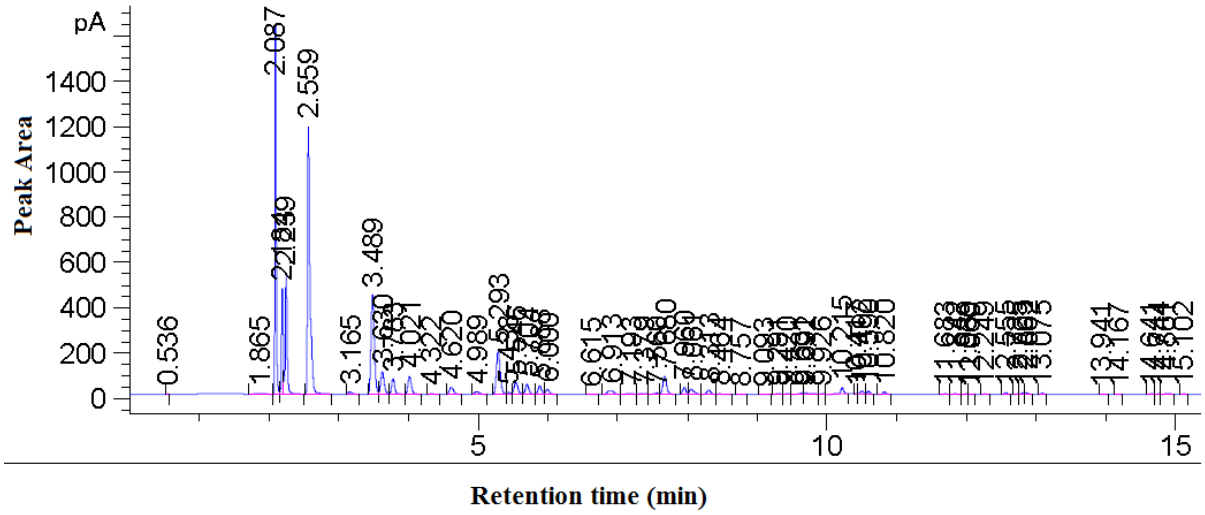


Figure 4.9: Typical gas chromatogram of the tail gas collected from the FTS experiment in this study.

4.2.4 The relationship between $P_{(n+1)}/O_{(n+1)}$ and $P_{(n)}/O_{(n)}$

In this work, the P/O ratio among different carbon numbers over Fe-Clino catalysts are shown in **Figure 4.10**. The figure shows the molar ratio of $P_{(n+1)}/O_{(n+1)}$ as a function of the molar ratio of $P_{(n)}/O_{(n)}$:

(1) With chain length n>2, $P_{(n+1)}/O_{(n+1)}$ versus $P_{(n)}/O_{(n)}$ follow a fairly good linear relationship, which can be described as follows:

$$\left.\frac{P_{(n+1)}/O_{(n+1)}}{P_{(n)}/O_{(n)}}\right|_{n>2} \approx ranges\ from\ 0.1995\ to\ 5.9548$$

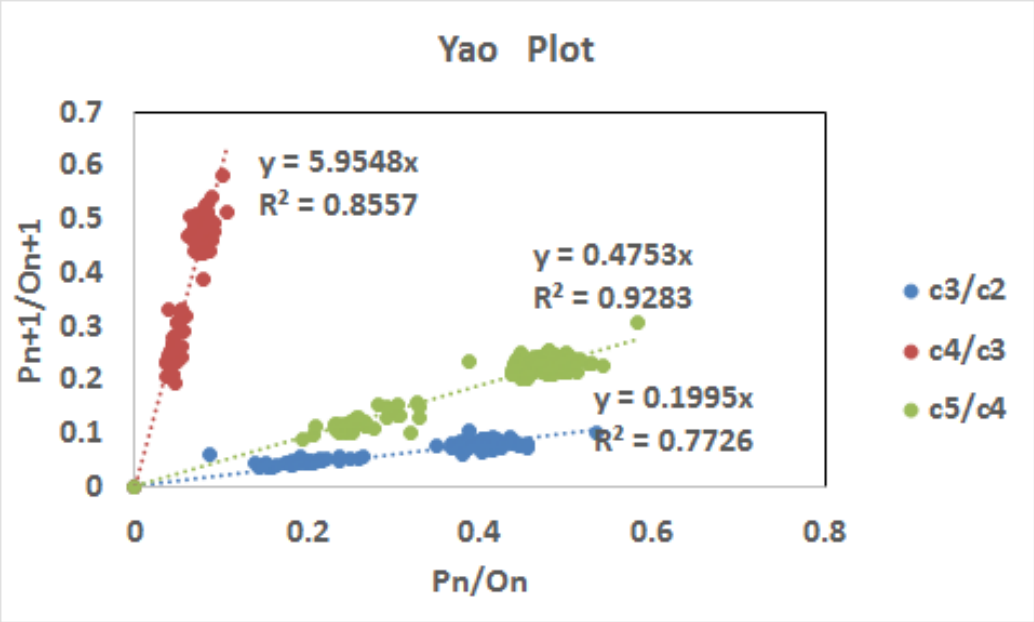


Figure 4.10: Yao Plots for $P_{(n+1)}/O_{(n+1)}$ versus P_n/O_n with carbon number n = 2–5

Table 4.8 gives a comparison of $(P_{(n+1)}/O_{(n+1)})/(P_n/O_n)$ calculated from Table 4.7 with gradients obtained from Yao plots (Figure 4.10**)**. One needs to appreciate the nearness of the values. As R^2 gets close to 1 the values from the Yao plots approach the calculated value. The significance of the patterns indicates the relationship between light hydrocarbons. But are these values anyhow related to the alpha values is the question yet to be answered?.

Table 4.8: Comparison of (P(n + 1)/O(n + 1))/(Pn/On) calculated from Table 4.7 with Yao gradients from Figure 4.10.

$\frac{P(n+1)/O(n+1)}{Pn/On}$		
	Values obtained from **Table 4.7**	Yao Gradients from **Figure 4.10**
$\frac{P_{C_3}/O_{C_3}}{P_{C_2}/O_{C_2}}$	0.2000	0.1995
$\frac{P_{C_4}/O_{C_4}}{P_{C_3}/O_{C_3}}$	6.0000	5.9548
$\frac{P_{C_5}/O_{C_5}}{P_{C_4}/O_{C_4}}$	0.4792	0.4753

According to Anderson[28,29], the product distribution of hydrocarbons in FTS can be described by the Anderson-Schulz-Flory (ASF) equation:

$$\frac{W_n}{n} = (1-\alpha)^2\alpha^{(n-1)}$$

The distribution depends on a single parameter, α, the probability that a chain will grow rather than desorb from the catalyst. α^{n-1} being the probability of adding n-1 carbons, and (1-α) is the probability of not adding a carbon and therefore terminating chain growth.

Where *Wn* is the mass fraction of a hydrocarbon (HC) with chain length *n* and the growth probability factor α is assumed to be constant. α determines the total carbon number distribution of the FT products. Thus, a plot of the logarithm of *Wn*/*n* versus *n* would produce a straight line plot whose slope is related to α. However, for most iron and cobalt

catalysts, marked deviations from this ideal distribution are observed. The product distribution for this condition follows a one alpha ASF distribution with an alpha value of 0.86.

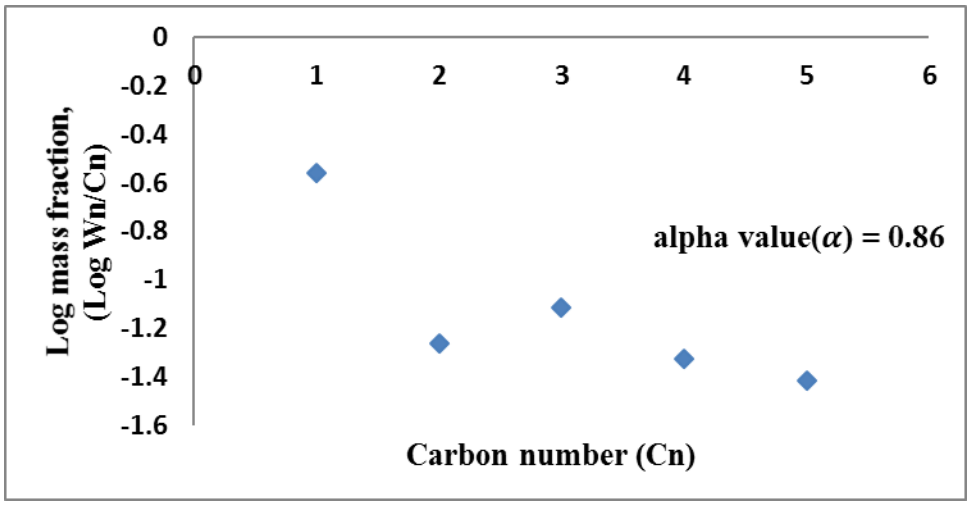


Figure 4.11: ASF distribution for light hydrocarbons

Since the experimental determination of α is somewhat arbitrary, the calculation of this parameter has been performed at different hydrocarbon numbers as proposed in the literatures.

References

[1] H.-Y. Lin, Y.-W. Chen, C. Li, Thermochim. Acta 400 (2003) 61–67.

[2] K. Mondal, H. Lorethova, E. Hippo, T. Wiltowski, S.B. Lalvani, Fuel Process. Technol. 86 (2004) 33–47.

[3] N. Dİlmaç, S. Yörük, Ş.M. Gülaboğlu, Metall. Mater. Trans. B Process Metall. Mater. Process. Sci. 46 (2015) 2278–2287.

[4] W.K. Jozwiak, E. Kaczmarek, T.P. Maniecki, W. Ignaczak, W. Maniukiewicz, Appl. Catal. A Gen. 326 (2007) 17–27.

[5] J. Gorimbo, Catal. Sci. Technol. (2018) 2022–2029.

[6] R.J.O. Brien, B.H. Davis, 94 (2004) 0–5.

[7] H. Wan, B. Wu, C. Zhang, H. Xiang, Y. Li, J. Mol. Catal. A 283 (2008) 33–42.

[8] H. Wan, B. Wu, X. An, T. Li, H. Xiang, Y. Li, Z. Tao, J. Nat. Gas Chem. 16 (2007) 130–138.

[9] G. Jacobs, P.M. Patterson, Y. Zhang, T. Das, J. Li, B.H. Davis, Appl. Catal. A 233 (2002) 215–226.

[10] E. Van Steen, M. Claeys, K.P. Möller, D. Nabaho, 549 (2018) 51–59.

[11] J. Gorimbo, EFFECT OF THE HOMOIONIC FORM OF CLINOPTILOLITE ON Ni 2 + ADSORPTION ISOTHERMS : A THERMODYNAMIC STUDY, UNiversity of the Witwatersrand, 2011.

[12] J. Liu, P. Wang, W. Xu, E.J.M. Hensen, 3 (2017) 467–476.

[13] A. Agostmo, Anal. Chim. Acta 262 (1992) 269–275.

[14] D. Song, J. Li, J. Mol. Catal. A Chem. 247 (2006) 206–212.

[15] Y. Yao, Fischer-Tropsch Synthesis Using Co 2 -Containing Syngas Mixtures Over Cobalt and Iron Based Catalysts, 2011.

[16] C.M. Masuku, Interaction between Reaction and Phase Equilibria in the Fischer–Tropsch Reaction, 2011.

[17] M.E. Dry, A.P. Steynberg, in:, Stud. Surf. Sci. Catal., 2004, p. 406.

[18] N.E. Tsakoumis, M. Rønning, Ø. Borg, E. Rytter, A. Holmen, Catal. Today 154 (2010) 162–182.

[19] J. Gorimbo, B. Taenzana, A.A. Muleja, Environ. Sci. Pollut. Res. (2018).

[20] P.P. Diale, E. Muzenda, J. Zimba, II (2011).

[21] E. de Smit, B.M. Weckhuysen, Chem. Soc. Rev. 37 (2008) 2758–2781.

[22] K. Keyvanloo, W.C. Hecker, B.F. Woodfield, C.H. Bartholomew, J. Catal. 319 (2014) 220–231.

[23] D.B. Bukur, L. Nowicki, S.A. Patel, Can. J. Chem. Eng. 74 (1996) 399–404.

[24] J. Gorimbo, A. Muleja, X. Liu, D. Hildebrandt, Int. J. Ind. Chem. 9 (2018) 317–333.

[25] G.A.O. Junhu, W.U. Baoshan, Z. Liping, Y. Yong, H.A.O. Xu, X.U. Yuanyuan, L.I. Yongwang, CHINESE J. Catal. 32 (2011).

[26] J.C. Mol, J. Mol. Catal. A 213 (2004) 39–45.

[27] X. Lu, Fischer-Tropsch Synthesis : Towards Understanding, 2011.

[28] A. Tavakoli, M. Sohrabi, A. Kargari, NSTI-Nanotech 4 (2007) 377–380.

[29] D. Förtsch, K. Pabst, E. Groß-hardt, Chem. Eng. Sci. 138 (2015) 333–346.

CHAPTER 5

Conclusions and recommendations

5.1 Conclusions

The primary objective of the research undertaken for this dissertation was to utilize the experimental findings to advance knowledge on the possibilities of using naturally occuring zeolites as catalyst support in FTS. Substantial progress has been made in this dissertation towards generating detailed knowledge on the use of clinoptilolite as a support.

XRD characterization of the natural zeolite identified the zeolite as clinoptilolite with hematite phases. XRF gave qualitative identification of the mineral content and chemical composition indicating molecular ratio SiO_2/ Al_2O_3 of Fe-Clino is about 5.96 which is quite ideal.

Experimental investigations were performed at laboratory scale using a fixed bed reactor and pressure 20.85 bar (absolute) and gas hourly space velocity of 2592 h^{-1} and fixed reactor temperature of 250 ^oC, where invaluable data were successfully collected and analysed for a TOS ca.450 h. The experimental work proved the possibility of the use of natural zeolites as supports.

The data obtained were analysed both qualitatively and quantitatively, in order to assess any unique trends in the product distribution. Based on the results and discussions presented the significance of using different models to yield different graphical plots such as Yao plots were investigated and the models seem to be quite useful.

It has been demonstrated that the use of ASF models, Yao plots including paraffin to olefin ratios is a promising approach for displaying product distribution in the FT process. Thus, the classical ASF model can be augmented with the newly introduced Yao plots to aid in explaining the product distribution. The experimental results show that the paraffin to olefin (P/O) ratios were strongly reflecting the selectivity of the catalyst.

The data collected in this project, though quite useful, remains valid only to the fixed bed type of reactors investigated. However, it is hoped that the project has given some impetus for further research, and where the analysis is inconclusive, it provokes further thinking for improvements. Thus, this dissertation is a contribution to the understanding of the FT process at using clinoptilolite as a support for iron based catalyst.

5.2 Recommendations

Catalyst Fe-clino showed more promising results with high activity and higher olefin selectivities comparative to other catalyst used in laboratory scale FTS. The catalyst displayed some negative results, chiefly its very low CO conversion. It would be interesting to tailor zeolites supports to have better or similar characteristics to commercially synthesised supports, for instance thermal treatment may improve porosity and increase surface area. Other preparation methods for the catalysts could be looked into. Using the incipient wetness method required the iron to be loaded on the support in multiple steps. This may have led to lower dispersions. By using other techniques, where the metal is loaded on to the support in one step, the activity could possibly be increased.

The research findings presented in this dissertation have made significant progress in terms of using clinoptilolite as a support. In order to have an in-depth understanding of the iron catalyst supported on clinoptilolite the following recommendations for further work/research are suggested.

1) There is need to test the behaviour of the catalyst supported on clinoptilolite with different reducing gases. A positive result in this regard would enhance the confidence required to use a certain gas as a reducing agent.

2) Assess the behaviour of the catalyst under different operating conditions viz low pressure, low space velocities and in different types of reactors (such as fluidized bed type reactors).

3) Test in-situ regeneration of the catalyst supported on the clinoptilolite.

Desirable characteristics of a catalyst support are stability, inertness, high surface area, porosity and appropriate chemical structure. Among a wide range of support materials investigated so far clinoptilolite can be tailed to meet optimally these characteristics. Supports keep the catalytic phase highly dispersed, thus protecting it from sintering and supported catalyst has shown better catalytic performance for catalytic processes.